

Novel Paradigms For Visual Field Mapping With Functional Magnetic Resonance Imaging

Yan Ma
Marquette University

Recommended Citation

Ma, Yan, "Novel Paradigms For Visual Field Mapping With Functional Magnetic Resonance Imaging" (2013). *Dissertations (2009 -)*. Paper 296.
http://epublications.marquette.edu/dissertations_mu/296

Novel Paradigms for Visual Field Mapping with Functional Magnetic Resonance Imaging

by

Yan Ma

A Dissertation submitted to the Faculty of the Graduate School,
Marquette University,
in Partial Fulfillment of the Requirements for
the degree of Doctor of Philosophy

Milwaukee, Wisconsin

August 2013

ABSTRACT

NOVEL PARADIGMS FOR VISUAL FIELD MAPPING WITH FUNCTIONAL MAGNETIC RESONANCE IMAGING

Yan Ma

Marquette University, 2013

The overall goal of this study is to evaluate the existing, and develop new visual field mapping paradigms, which consist of visual stimulation scheme, post-processing and displaying tools using fMRI for both research and clinical applications.

We first directly compared phase mapping and random multifocal mapping paradigms with respect to clinically relevant factors. Multifocal mapping was superior in immunity to noise and was able to accurately decompose the response of single voxels to multiple stimulus locations. In contrast, phase mapping activated more extrastriate visual areas and was more efficient per run in achieving a statistically efficient response in a minimum time but required separate runs to map eccentricity and angle. Multifocal mapping became less efficient as the number of simultaneous stimulus locations increased from 13 to 25 to 49 and when duty cycle increased from 25% to 50%. In sum, each paradigm offers advantages that may be optimal for different applications.

Given the respective advantages and weaknesses of phase-encoded design and random multifocal design, we further developed a novel paradigm by combining the phase-encoded stimuli and one or two isolated random segments. The addition of the random stimuli was shown to have insignificant effect on the retinotopic mapping by the phase-encoded stimuli. Three applications were demonstrated for this combined paradigm: Simultaneous mapping the retinotopy and selected ROIs, automated calibration of the temporal phases, and delineation of the hemodynamic response function for selected voxels.

At present the representation of the visual field by the visual cortex is displayed as a diagram of a subject's visual field with circular symbols placed at locations to which voxels have shown a response. The diagram provides an intuitive way of interpreting the fMRI cortical maps in terms of visual function. However, it provides little information about the relative probability of obtaining a brain response from different locations within the field of view. Therefore, we derived a quantitative form of such a diagram, on which a probability distribution could be drawn. The quantitative diagrams from five subjects showed highly variable patterns of coverage, which made it questionable whether any meaningful probabilistic distribution can be obtained.

ACKNOWLEDGEMENTS

Yan Ma

I would like to express my gratitude to my committee members Dr. Edgar DeYoe, Dr. Kristina Ropella, Mr. Doug Ward, Dr. Brian Schmit, Dr. Scott Beardsley, Dr. Ziad Saad and Dr. Shi-jiang Li for their invaluable knowledge and insightful suggestions. In particular, I would like to thank Dr. Edgar DeYoe, Dr. Kristina Ropella and Mr. Doug Ward for their exceptional mentoring and encouragement. My thanks also go to Jed Mathis for his generous technical support, Danielle Reitsma, Andy Salzwedel and Alex Puckett for numerous inspiring discussions, and Patricia Smith and Mary Wesley for administrative assistance.

Special thanks to my parents, grandparents and aunties for their unconditional love and their support for my decision to pursue a graduate career, which turned out to be one of best decisions I've made in my life. I'd also like to thank my husband, Xinyang Hu, who left his life behind and came here for me. I deeply appreciate it.

Last but not least, I would like to thank my friends for the good and bad times we had together. You helped and inspired me in many different ways!

TABLE OF CONTENTS

ACKNOWLEDGEMENTS.....	i
TABLE OF CONTENTS	ii
LIST OF TABLES.....	v
LIST OF FIGURES.....	vi
PREFACE	viii
SPECIFIC AIMS.....	x
CHAPTER 1 BACKGROUND AND SIGNIFICANCE	1
<i>Basic organizational principles of human visual cortex</i>	<i>1</i>
<i>Blood Oxygenation Level Dependent (BOLD) Functional Magnetic Resonance</i>	
<i>Imaging (fMRI)</i>	<i>5</i>
<i>Motivation for visual field mapping.....</i>	<i>8</i>
<i>Mapping the Visual Field</i>	<i>10</i>
CHAPTER 2 GENERAL EXPERIMENTAL METHODS	15
<i>Apparatus for visual stimulation.....</i>	<i>15</i>
<i>Magnetic resonance imaging</i>	<i>15</i>
<i>Functional field map (FFMap) calibration.....</i>	<i>16</i>
CHAPTER 3 COMPARISON OF RANDOMIZED MULTIFOCAL MAPPING AND TEMPORAL	
PHASE MAPPING.....	18

<i>Introduction</i>	<i>18</i>
<i>Material and methods</i>	<i>23</i>
<i>Results.....</i>	<i>32</i>
<i>Discussion.....</i>	<i>47</i>
 CHAPTER 4 VISUAL FIELD MAPPING COMBINING PHASE-ENCODED AND EVENT-RELATED STIMULI.....	56
<i>Introduction</i>	<i>56</i>
<i>Methods.....</i>	<i>59</i>
<i>Results.....</i>	<i>69</i>
<i>Discussion.....</i>	<i>77</i>
 CHAPTER 5 IMPROVE THE SENSITIVITY AND RELIABILITY OF FUNCTIONAL FIELD MAPS FOR DETECTION OF SCOTOMATA	82
<i>Introduction</i>	<i>82</i>
<i>Methods.....</i>	<i>84</i>
<i>Results and discussion.....</i>	<i>86</i>
<i>Conclusion.....</i>	<i>92</i>
 CHAPTER 6 SUMMARY AND FUTURE DIRECTIONS	94
<i>Scale contrast of the combined stimuli to reflect the linearity</i>	<i>95</i>
<i>Other possible combined stimuli.....</i>	<i>95</i>
<i>Further experiments with quantitative FFMaps.....</i>	<i>96</i>

REFERENCE	97
-----------------	----

LIST OF TABLES

Table 1.....	47
Table 2.....	60
Table 3.....	74

LIST OF FIGURES

Figure 1.....	3
Figure 2.....	12
Figure 3.....	21
Figure 4.....	28
Figure 5.....	34
Figure 6.....	37
Figure 7.....	38
Figure 8.....	40
Figure 9.....	43
Figure 10.....	44
Figure 11.....	45
Figure 12.....	46
Figure 13.....	50
Figure 14.....	62
Figure 15.....	64
Figure 16.....	65
Figure 17.....	70
Figure 18.....	72
Figure 19.....	76
Figure 20.....	77
Figure 21.....	86
Figure 22.....	87
Figure 23.....	88

Figure 24.....	90
Figure 25.....	91

PREFACE

What does it mean to see? The plain man's answer would be, to know what is where by looking. In other words, vision is the process of discovering from images what is present in the world, and where it is (Marr, 1982). Vision therefore requires encoding of the spatial structure of the images. The spatial arrangement of the visual field is preserved in the topographical arrangement of photoreceptors in the retina, and carried on in the subsequent visual pathways through the primary visual cortex and some of the higher visual areas.

Functional magnetic resonance imaging (fMRI), which shows localized changes in blood flow and oxygenation evoked by changes in neural activity, is the primary technique for mapping the spatial structure of the human visual field. A visual field mapping paradigm, which includes a visual stimulation scheme, post-processing routines and result presentation tools, is created to map the visual field efficiently and reliably, so that visual field mapping could be used not only for research, but also for clinical applications. Thus, the overall goal of this study is to evaluate and enhance fMRI-based visual field mapping paradigms for clinical use.

Several specific issues are addressed. The first issue was to establish the respective merits of the most widely accepted phase-encoded paradigm versus a promising multifocal paradigm. These two paradigms have fundamentally different encoding schemes, which have not been directly compared before. Quantitative comparison of the two paradigms not only provides a reference for investigators who use visual field mapping as tool, but also helps establish a deeper understanding of the working principles of human visual cortex. Secondly, we developed a novel visual field mapping paradigm by combining phase-encoded stimuli and event-related stimuli

(multifocal stimuli are presented using event-related temporal sequences). The concept of combining visual stimuli with different temporal structures and thus different strengths was put into practice for the first time. This combined paradigm was shown effective in three different applications. Finally, we explored the potential for a new type of display of the mapping results, which shows the probability of obtaining a brain response from different locations within the visual field.

In Chapter 1 we present an overview of the relevant background including basic organizational principles of human visual cortex, blood oxygenation level dependent fMRI, the rationale for visual field mapping and various techniques for achieving such mapping. In Chapter 2 the experimental and post-processing methods common to all three aims are presented. Detailed description and discussion of the three aims are then presented in subsequent Chapters 3-5. An overall summary and future directions are discussed in Chapter 6.

Overall this thesis provides an in-depth assessment of the most influential visual field mapping paradigms used in the field and implements a new design concept. Our results offer a useful reference for selecting different visual field mapping techniques and explore different methods to optimize these techniques for clinical use.

SPECIFIC AIMS

Aim 1 (Chapter 3). Compare random multifocal and conventional phase-encoded visual field mapping paradigms with respect to effectiveness and time efficiency.

Conventional phase-encoded visual field mapping identifies a voxel's responding location by the phase of the voxel's signal, while random multifocal mapping makes such identification by the temporal pattern of the voxel's signal. The respective merits of the two encoding mechanisms were generalized through quantitative comparison.

Aim 2 (Chapter 4). Develop and test a combined visual field mapping paradigm that takes advantage of both phase-encoded and event-related designs.

We created a new visual stimulation paradigm, which consisted of phase-encoded stimuli moving sequentially in space and event-related stimuli turning on and off randomly at fixed locations. The two types of stimuli were designed to be perceptually independent to achieve separation of the signals evoked by either one. Three potential applications were demonstrated for this new paradigm.

Aim 3 (Chapter 5). Develop a prototype of a probability-based FFMMap and evaluate its potential for clinical use.

Current FFMMaps were first updated by incorporating information about pRF sizes estimated using a pRF modeling process proposed by Dumoulin and Wandell (Dumoulin and Wandell, 2008) to achieve more quantitative representation of the coverage of the visual field within visual cortex. As a premise for a probability-based FFMMap, quantitative FFMMaps were generated but showed high variation in the distribution of pRFs throughout the visual field and across subjects. Such variability makes it questionable whether a probabilistic FFMMap is currently feasible.

CHAPTER 1 BACKGROUND AND SIGNIFICANCE

Basic organizational principles of human visual cortex

The primate visual system is not only capable of identifying and locating objects, but also of producing perception of 3D form, surface properties, 3D spatial relationships, and 3D movement from a 2D retinal image (DeYoe and Van Essen, 1988). It is necessary to lay out the general organization of human visual system before addressing the specific visual field mapping techniques. The human visual system is composed of several distinct sub-systems including: 1) the geniculo-striate system for conscious visual perception, 2) the retino-tectal system for directing eye movements and visual attention, 3) the pupillary control system for adjusting light intensity, and 4) the accommodation control system for focusing the eye, etc (DeYoe and Van Essen, 1988; Kandel et al., 1991). This research focuses on those components of the human visual system within cerebral cortex that are readily accessed by neuroimaging and, therefore, can be used to guide patient diagnosis and treatment.

Retinotopic organization

The spatial organization of the visual field is preserved in the topographical arrangement of photoreceptors in the retina, and carried on in the subsequent visual pathways through the primary visual cortex and some of the higher visual areas. As shown in the top row of Figure 1, the center of gaze (fovea), colored blue, is located at or near the posterior pole of the occipital lobe of each hemisphere, with the far peripheral field, colored hot pink, represented more anteriorly near the junction of the calcarine and

parieto-occipital sulci. Normally, the primary visual cortex contains a map of the visual field which is upside down and backwards compared to the visual field. This is illustrated in the bottom row of Figure 1, where the right half of visual field is represented in the left hemisphere, and the lower vertical meridian, colored orange, corresponds to the upper bank of calcarine sulcus. However, this brain map is disproportional to the actual visual field in that portions of the visual field that are close to the center of gaze subtend an increasingly larger area of the cortex, thus reflecting the better visual acuity and critical importance of foveal vision (Horton, 1992). The “cortical magnification” of the center of gaze can be explained by the much finer spatial sampling of fovea than peripheral visual field throughout stages of visual processing (Duncan and Boynton, 2003). Thus an increasingly larger stimulation pattern, indicated by increased spacing between eccentricities in the top visual field graph in Figure 1, is usually used from fovea to peripheral field to stimulate similarly sized patches of cortex. The phenomenon of cortical magnification is clinically significant in that large lesions at or near the posterior occipital cortex can cause relatively small sized deficits in the visual field, yet, the small-sized deficits can cause major impairment of reading and other functions that require high visual acuity. Conversely, lesions of the anterior occipital cortex can cause blindness in large portions of the peripheral visual field, but the deficit may be well-tolerated or even unnoticed by the person with the lesion.

The red circle in the graph on the right of Figure 1 indicates the region of visual field that when stimulated, activates the corresponding voxel in visual cortex. In other words, it is the combined spatial receptive fields of the neurons in a voxel, termed the voxel’s population receptive field (pRF). In accordance with the principle of “cortical magnification”, the pRFs are relatively small for voxels representing the fovea and increase in size with eccentricity (Dumoulin and Wandell, 2008; Kastner et al., 2001;

Smith and Strottmann, 2001; Tootell et al., 1997).

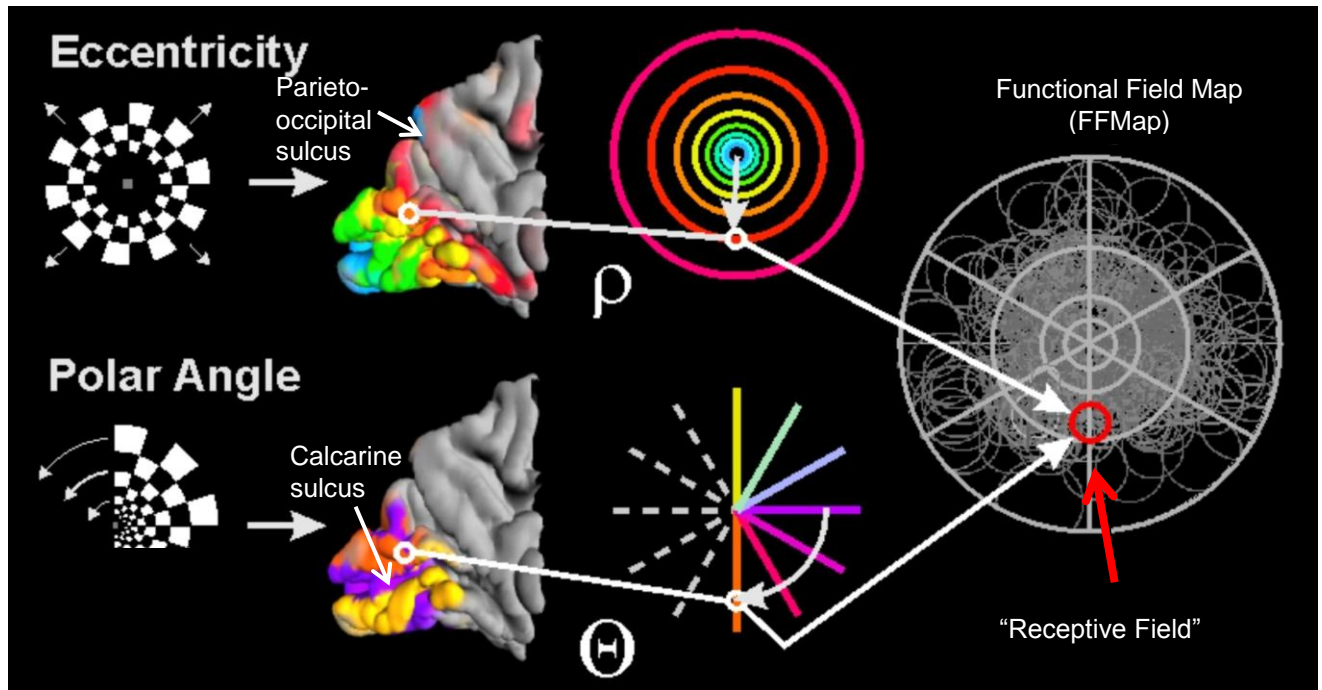


Figure 1. Conventional temporal phase-based visual field mapping. Top row: Eccentricity mapping. Bottom row: Polar angle mapping. Columns from left to right: visual stimulation, human hind brain model, visual field diagram, functional field map (FFMap).

Multiple visual areas

fMRI brain maps reveal several representations of the contralateral hemifield in each hemisphere, i.e. right hemifield is represented several times in left hemisphere and so is the left hemifield in the right hemisphere. See Figure 3 for the layout of these representations on cortical surface models. The one representation at medial occipital lobe is known as striate cortex or primary visual area, V1, which is the largest of these visual areas. Thus it has a visual field representation with the highest spatial resolution. Lesions of V1 typically produce localized areas of blindness, termed scotomata.

Additional extrastriate visual areas are located in the occipital lobe and adjacent portions of parietal and temporal lobes. They are implicated in the processing of different visual attributes, like motion, form, color, faces and etc. Damage to higher extrastriate visual areas beyond V2 or V3 does not produce blindness, but rather a specific perceptual loss of one or more visual attributes. Meanwhile, it is likely that more than one map is essential for a particular visual function and that each individual map participates in multiple functions.

The arrangement of multiple retinotopic maps is perhaps dictated by the importance of combining information from nearby locations in the visual field to many cortical visual functions (motion, form, color, faces and etc.). The organization of these maps has been explained by two influential hypotheses (Wandell et al., 2007). The first hypothesis was raised by Ungerleider et al. in 1982 (Ungerleider et al., 1982) after they found that projections from V1 are carried via two major white matter pathways toward ventral and dorsal extrastriate cortex. They hypothesized that the ventral pathway is specialized for “identifying what an object is” and the dorsal pathway is specialized for “locating where an object is” based on the different deficits caused by lesions to the two different pathways. A second important organization was developed by Van Essen et al. by noting the relationships between visual areas as ascending (forward), descending (feedback) and lateral according to laminar patterns of connections between areas (Felleman and Van Essen, 1991). They further proposed an anatomical hierarchy that contained 14 levels of processing including retina and lateral geniculate nucleus at the bottom, 10 levels of cortical processing and entorhinal cortex and hippocampus at the top. Multiple, intertwined processing streams are present within this hierarchy.

It is an ongoing effort to describe the overall functional and structural organization of visual areas. New hypotheses have been proposed as the field evolves

(Levy et al., 2001; Wandell et al., 2005). It is important to note that these hypotheses are tentative and none of them are mutually exclusive.

Blood Oxygenation Level Dependent (BOLD) Functional Magnetic Resonance Imaging (fMRI)

In this study we used BOLD fMRI as our primary research tool to study the brain response to various visual stimulations. In this section, we aim to present an overview on various aspects of this technique that are of direct relevance to this study.

Basic mechanism of BOLD

BOLD was first introduced as a contrast mechanism for magnetic resonance imaging in 1990 by Ogawa et al. (Ogawa et al., 1990a; Ogawa et al., 1990b; Ogawa and Tso-Ming, 1990). It depicts changes in concentration of deoxyhemoglobin induced by neural activity, thus providing measurements related to regional neural activity. In short, regions of the cerebral cortex that are active require additional oxygen for metabolism. The increased oxygen supply by the vasculature and consumption by the active cortex do not match precisely. The net result is that the active cortex has less deoxyhemoglobin, and thus a more homogeneous magnetic field. Hence, active cortex has an increased local MR signal due to the more homogenous local magnetic field. The capability of measuring neural activity adds the feature of imaging brain functions to MRI, which leads to the name “functional MRI”. Since its discovery, BOLD fMRI has become the most widely used method for human brain imaging for its good coverage, high spatial resolution and non-invasive nature. Routine fMRI scans with a 3 tesla scanner provide 2 mm isotropic voxels at the Medical College of Wisconsin. With the numerous advancements in pulse sequences, hardware, processing tools and

experimental designs in the past twenty years, fMRI has grown and will continue to grow in usage, sophistication, range of applications, and impact (Bandettini, 2012).

Physiological correlates of BOLD

While BOLD fMRI has proved itself to be a powerful and versatile tool for the study of the neural activities, it is still unclear that how it is coupled to the underlying neurophysiology (Singh, 2012). To understand the relationship between the BOLD signal and its underlying neural events, it is necessary to comprehend the neurophysiological signals commonly reported in animal studies. Three common types of such signals are single-unit activity representing the action potentials of well isolated neurons next to the electrode tip, multiple-unit activity representing the spiking of small neural population in a sphere of 100-300 μm radius, and perisynaptic activity of a neural population within 0.5-3 mm of the electrode tip, which is reflected in the variation of the low-frequency components of the extracellular field potential, termed local field potential (LFP) (Logothetis, 2008). Quantitative analysis indicated that LFPs are better predictors of the BOLD response, particularly in the gamma range (Logothetis et al., 2001), than multiple-unit or single-unit spiking (Logothetis, 2002).

Alternatively non-invasive electroencephalography (EEG) and magnetoencephalography (MEG), which provide signals representing the synchronous activity of many square millimeters or centimeters of cortex, have also been used in conjunction with fMRI to find the electrophysiological signals that seem to match the BOLD response. A large number of studies have focused on the gamma band based on previous literature linking BOLD to gamma responses. The collective findings of this field suggested that although BOLD and induced gamma oscillations occur at the same location during the task, the BOLD response may only be partially correlated with these

gamma responses (Singh, 2012).

BOLD fMRI has become an incredibly useful and popular tool for neuroscience even with the ambiguous neurophysiological origin. This is largely attributable to the linearity of the BOLD signals. Specifically, the time-course of the fMRI response can be predicted by convolving the time-course of the neuronal response with a hemodynamic impulse response, followed by additive Gaussian noise.

Since the introduction of fMRI to the field of neuroscience, the linearity of BOLD signal has been studied intensively due to its importance in modeling and analyzing fMRI signals. Nearly all fMRI data analysis techniques assume or require linearity (Boynton et al., 2012). It is remarkable that the BOLD mechanism has been shown to be a linear time-invariant system by various groups despite of the complex and still unclear physiological basis of the BOLD signal (Boynton et al., 1996; Dale and Buckner, 1997). However, apparent nonlinearity was observed for brief stimuli in both visual system (Birn et al., 2001) and auditory system (Robson et al., 1998). Birn et al found that the fMRI response to a 250 ms visual stimuli can be 3-5 times larger than what is expected from a longer stimulus. Spatial linearity was also demonstrated in human V1 by an experiment involving spatial summation, with the caveat that smaller stimuli, nonlinear underlying neural response and specific experimental design could cause spatially nonlinear fMRI responses (Hansen et al., 2004).

Linearity of the fMRI signal has enabled the emergence of rapid event-related experimental designs. In a typical event-related design, different types of events or conditions are presented in a pseudo random order, resulting in an fMRI signal that contains the sum of responses to individual events. The hemodynamic response function for each event is then found through deconvolving the fMRI signal to the time-course of the stimulus, which relies heavily on the assumption of linearity (Boynton et al.,

2012).

In addition to the ambiguity in neurophysiological origin, one other major limitation fMRI suffers is the low temporal resolution. The usual temporal resolution on the order of seconds is far from satisfactory for some cognitive events that can happen within milliseconds. In cases where temporal resolution is critical multi-modality imaging combining fMRI with other imaging modalities that offer high temporal resolution, such as EEG/MEG, could be performed (Liu and He, 2008; Taylor et al., 2012).

Motivation for visual field mapping

Visual field mapping is to find out the cortical voxels responsive to visual stimulation within different regions of the visual field, thus generating a map of the visual field on the cortex. This study aims to evaluate the existing, and develop new presentation schemes of visual stimulation to map the visual field. Motivations for visual field mapping for both scientific research and clinical diagnosis and treatment are reviewed in this section.

For scientific research

For scientific research the foremost goal of visual field mapping is to understand the mechanism of cortical processing of vision, given that the relationship between maps and perception is neither direct nor unique (Wandell et al., 2007). The quantitative measurements of the visual field maps in humans can also shed some light on the homology with non-human primates, who have a wealth of literature describing their visual field maps quantitatively (Van Essen, 2003). In addition, visual field maps provide a way of identifying functionally equivalent regions across subjects, thus enabling the

comparison or combination of data of different subjects. This usage of visual field maps is important due to the variable anatomical structures across people (Wandell et al., 2007). Finally, visual field mapping with fMRI can also be used for detailed analyses of abnormalities within visual system. Invaluable insights of the visual system can be learned through studying the “alternative” conditions provided by these abnormalities. In fact it has been shown useful in a large variety of clinical disorders, including inherited photoreceptor abnormalities (Baseler et al., 2002), amblyopia (Conner et al., 2007), glaucoma (Duncan et al., 2007a), albinism (Hoffmann et al., 2003), achiasma (Sinha and Meng, 2012), scotoma (Sunnness et al., 2004), long-period deprivation of visual input (Levin et al., 2010) and developmental reorganization of cortical visual field maps (Muckli et al., 2009). It has also played an important role in the large debates on cortical plasticity (Baseler et al., 2011).

For Clinical diagnosis and treatment

Clinically prior to surgical treatment of tumors and other types of focal pathology, fMRI visual field mapping is used to identify areas of the brain that might be at risk if the surgery damages functioning brain tissue. For tumors of the occipital lobe or adjacent portions of the parietal or temporal lobes, damage to visual cortex may lead to partial blindness or other disruptions of vision.

Although fMRI mapping of the visual field can provide key information affecting diagnostic or treatment decision in pre-surgical mapping, it is still rarely performed clinically. In part, this may reflect a lower incidence of tumors and other pathologies in posterior portions of the brain. This may also reflect a lack of awareness of the potential benefits and clinical uses of visual system mapping, and the relative ease with which useful fMRI data can be obtained. Technically there are several impediments for

applying visual field mapping in clinical settings. First, the optimal visual field mapping techniques are different for research purposes than for clinical use. Research studies may benefit from selective delineation of different functional areas to better understand human visual processing, while clinicians usually prefer complete depiction of the whole visual system to guide surgical resections. Second, clinical patients with different kinds of pathologies may have difficulty performing certain complex functional tasks which could be easily performed by healthy adults. Even the most basic requirement of fMRI scans, lying still, could be somewhat challenging for patients. Third, time efficiency is particularly important in clinical applications. Here time efficiency refers to both the time duration needed to complete a single scan session and the total time period needed to achieve a clinical decision, e.g. acquire sufficient information to make a diagnosis or treatment plan (DeYoe et al., 2011). Given these different demands for clinical applications of a diagnostic test, a time efficient fMRI visual field mapping paradigm that works reliably in all visual areas is desirable.

Mapping the Visual Field

Pre-fMRI

The first visual field map, V1, was discovered by Inouye and Holmes a century ago. World War I produced a large number of isolated missile wounds of the brain. Their study yielded a complete topographical mapping of the visual field in the primary cortical vision center, and is the basis of our modern interpretation of visual fields (Fishman, 1997). Subsequently more visual field maps were uncovered in animal experiments using electrophysiological recordings, where the positions of the receptive fields of single neurons or small clusters of neurons were related to the locations of the corresponding

recording sites in the cortex to determine the representations of the visual field in the cortical areas (Cowey, 1964; Hubel and Wiesel, 1965; Talbot and Marshall, 1941; Tusa et al., 1978; Zeki, 1971). The difficulty of establishing a visual field map using single/multiple-unit recording mainly lies in the small field of view these techniques provide. The process of using electrodes to identify a map was described as “a dismaying exercise in tedium, like trying to cut the back lawn with a pair of nail scissors” (Hubel and Wiesel, 2004; Wandell and Winawer, 2011).

The V1 map was measured in the living human brain using positron emission tomography (PET) in 1980s (Fox et al., 1987). The regional cerebral blood flow was measured with the help of an extraneous tracer while different locations of the visual field were stimulated. The PET images served as evidence of the basic properties of V1 inferred from lesion studies in human and electrophysiological studies in non-human primates, although the coarse spatial resolution (18 mm FWHM after image reconstruction) and low signal-to-noise ratio limited their usefulness in further delineation of visual field maps. These limitations can be appreciated in Figure 2 (reprinted from Fox et al, 1987). See Figure 5 for representations of the visual field in fMRI images.

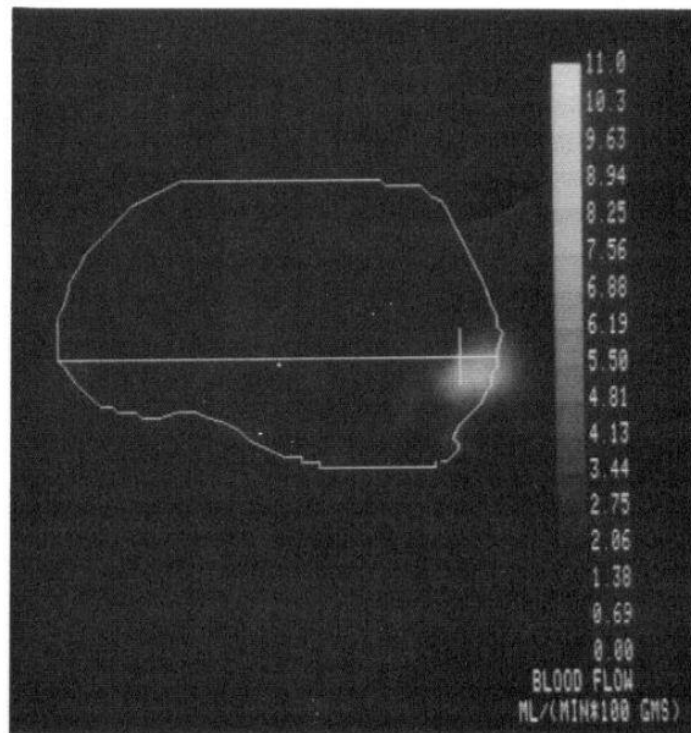


Figure 2. The PET image resulted from subtraction of the resting-state image from the stimulated-state image to macular stimulus. Reprinted from Fox et al, 1987.

Other criteria were also developed to parcellate visual cortex into visual areas before the advent of fMRI. The identification of distinct visual areas is generally based on finding reliable differences in one or more characteristics related to (i) architecture, (ii) connectivity, (iii) visual topography, and/or (iv) functional characteristics (Van Essen, 2003).

fMRI

It was only after the introduction of fMRI in the early 1990s that researchers could measure multiple visual field maps efficiently in healthy human brain. The classic

retinotopic mapping paradigm, phase-encoded mapping (DeYoe et al., 1996; Engel et al., 1997; Sereno et al., 1995), was invented shortly after the discovery of BOLD effect and is still widely used today. In this method, eccentricities/polar-angles are stimulated sequentially by contrast patterns in rings/wedges. The most effective eccentricity/polar angle for each voxel was identified by the phase of the voxel's response. The popularity of phase-encoded mapping lies in its efficient mapping of the entire visual field and the high SNR it offers. The specific advantages and limitations of phase-encoded mapping, a model-based post-processing technique and a novel stimulation paradigm with fMRI are discussed in detail in Chapter 3.

Currently the V1–V3 cortical maps have been found using fMRI in nearly every subject by every skilled experimental group (Winawer et al., 2010). In contrast, no group reports measuring all the extrastriate maps every time in every subject. There are several reasons for the difficulty in measuring maps beyond V1–V3. First, these maps are generally smaller than V1–V3 (Wandell et al., 2007). Second, in extrastriate regions, the pRF becomes progressively larger through the hierarchy of visual areas (Dumoulin and Wandell, 2008; Kastner et al., 2001; Smith and Strottmann, 2001; Tootell et al., 1997). When the pRFs of adjacent voxels overlap, stimuli in adjacent visual field positions produce only a small response difference, which makes the differentiation between them more difficult. Third, extrastriate maps appear to be more selective to specific types of stimuli, and we are not yet certain about the most effective stimuli to use for measuring these maps. Fourth, investigators are still discovering instrumental and biological limitations of the measurements. Some maps are located in hard to measure places, such as near the ear canals; other maps (or parts of maps) are near large veins that introduce MR artifacts that limit the ability to measure cortex (Wandell and Winawer, 2011; Winawer et al., 2010).

Multi-modality imaging of the visual cortex

A weakness of fMRI measurements is the relatively low temporal resolution. The response of the vasculature is on the order of seconds while the response of the nervous system is on the order of milliseconds (Wandell and Winawer, 2011). Therefore, various groups have worked to integrate time-resolved imaging modalities, such as electroencephalography (EEG) and magnetoencephalography (MEG), with fMRI. EEG recordings in visual areas defined by fMRI have contributed to identify two networks for figure and background processing in human visual cortex (Appelbaum et al., 2006). Knowing the responses arise in occipital cortex, and the solutions are like to be grouped within visual field maps, provides useful constraints for the selection of EEG sources (Wandell and Winawer, 2011).

Transcranial magnetic stimulation (TMS) has also been combined with fMRI to provide additional information that link activation within a particular cortical region to perception or behavior (Krings et al., 2001). TMS is a non-invasive technique that can cause depolarization or hyperpolarization in the neurons of the brain by inducing weak electric currents using a rapidly changing magnetic field. This brings localized, transient disruption of cortical function and can induce functional impairments in the performance of specific tasks with minimal discomfort. When guided by the detailed localizing and mapping capabilities of fMRI, TMS can be used as a means by which the functional roles of different visual areas can be investigated (McKeefry et al., 2009). However, a major shortcoming of TMS, the limited knowledge concerning its physiological effect, often makes the interpretation of TMS results difficult (Sack and Linden, 2003).

CHAPTER 2 GENERAL EXPERIMENTAL METHODS

For visual field mapping experiments, we created each visual stimulation pattern by programming a graph generator in MATLAB. The visual stimuli were presented to subject through an MRI-safe apparatus while fMRI images were acquired. The resulting images were then processed for statistical tests or display of the visual function.

Apparatus for visual stimulation

Visual stimulation was achieved using a custom back-projection system providing a 20° radius field of view. Custom computer graphical images were generated using a Cambridge Research System ViSaGe visual stimulus generator and displayed via a Sharp XG-C330X color video projector. All stimuli consisted of 8 Hz flickering checkerboard patterns with black/white contrast of 96% superimposed on a uniform gray background of 265, cd/m². Luminance levels for black and white checks were 23 and 1120, cd/m² respectively. Subjects were asked to passively fixate on a green marker within 0.1° radius of the center of the display throughout the stimulus presentation.

Magnetic resonance imaging

MRI scans were performed with a long bore scanner and a short bore scanner.

The long bore scanner is a 3T General Electric Signa Excite 3.0 MRI system equipped with an 8 channel High Resolution coil. A 96 x 96 voxel matrix covering a 24 x 24 cm field of view and 25 slices was used to obtain 2.5 mm³ voxels. A vendor-supplied, gradient-recalled EPI pulse sequence was used for fMRI imaging. The MR parameters were as follows: 77° flip angle, TR of 2000 ms, and TE of 30 ms. The first 4 images of

each scan, acquired while a uniform gray stimulus was displayed, were discarded to allow brain tissue magnetization to achieve steady state. A high resolution, T1-weighted, spoiled GRASS (gradient-recalled at steady state) anatomical image was also collected. The anatomical data set covered the whole brain with a voxel size of 0.9375mm x 1.0714mm x 1.0mm (flip angle = 12°, TR = 8.2 ms, TE = 3.2 ms).

The short bore scanner is a 3T GE Excite MRI scanner equipped with a 32 channel coil, where 29 axial slices were obtained for an fMRI volume. The same voxel matrix, field of view and slice thickness were used to achieve the same voxel size. A gradient-echo EPI pulse sequence with the same TE, TR and flip angle setup was used to collect the fMRI data. SPGR anatomical images were acquired with the same parameters and yielded the same voxel size.

Raw MRI data were converted into image format using GE Signa software and assembled into a time series of volumetric imaging data using the AFNI analysis package (Cox, 1996). Head motion correction was applied using AFNI's 3dvolreg routine, which registered each volume of images at each time point to the base volume. The base volume was selected to be 50th volume of the functional data set that was collected closest to the collection of SPGR. (Detailed description of each AFNI function used in this paper is available at AFNI website http://afni.nimh.nih.gov/pub/dist/doc/program_help/). The first 4 images of each scan, acquired while a uniform gray stimulus was displayed, were discarded to allow brain tissue magnetization to achieve steady state.

Functional field map (FFMap) calibration

The raw phase estimation made by temporal phase mapping is determined not only by the stimulus delay, but also by the hemodynamic delay. The raw phases need to

be calibrated to only represent the effect of stimulus delay. One way to calibrate the phases is through the use of a functional field map (FFMap).

An FFMap is a diagram of a subject's visual field with circular symbols placed at locations to which voxels have shown a response. Such a diagram is created to directly view the sensitivity profile of the visual cortex from fMRI response. An example of the FFMap is shown on the right side of Figure 1. The preferred stimulus eccentricity and angle for each voxel were first estimated from the uncorrected angle and eccentricity phase data, and used to place a circular symbol in the FFMap. Since medial occipital voxels from one hemisphere primarily respond to the contralateral visual field, the temporal phase measurements were then adjusted by a constant factor so that the symbols from each hemisphere were symmetrically distributed with respect to the vertical meridian. A comparable adjustment was also made to the eccentricity phase data and cross-checked to ensure that V1 voxels activated by foveal stimuli were at or near the occipital pole. The corrected polar angle and eccentricity phase data were then used to identify the final preferred stimulus location for each voxel.

CHAPTER 3 COMPARISON OF RANDOMIZED MULTIFOCAL MAPPING AND TEMPORAL PHASE MAPPING

In this chapter, we aim to compare random multifocal and conventional phase-encoded visual field mapping paradigms with respect to effectiveness and time efficiency.

Introduction

Functional magnetic resonance imaging (fMRI) is being used increasingly for mapping key brain structures prior to surgical treatment of tumors and other types of focal pathology. In such applications, the goal is to identify viable areas of the brain that might be at risk of damage due to resection, radiation or other invasive treatment of a pathology site. For tumors of the occipital lobe or adjacent portions of the parietal or temporal lobes, damage to visual cortex can cause partial or complete blindness or other disruptions of visual perception (Martin et al., 2012). Clinically, time efficiency is generally the most important design requirement for a visual field mapping paradigm in that it is usually difficult for patients to stay in MRI scanner for more than one hour. Requirement on other design aspects, such as spatial resolution, is minimal, i.e. only need to differentiate between fovea and periphery.

Temporal phase mapping

Conventionally, cortical maps of the visual field are charted using a temporal phase mapping technique that consists of a rotating checkered wedge, or an expanding checkered ring stimulus (Figure 3 A, B) (DeYoe et al., 1996; Engel et al., 1997; Engel et al., 1994; Sereno et al., 1995). Temporal phase mapping can evoke robust responses in

primary visual cortex (V1) and a number of extrastriate visual areas. Moreover, the checkered ring stimulus can identify locations in visual cortex that support central vision, which if damaged can impair reading and other critical visual functions. The ability to identify central vision makes temporal phase mapping particularly useful for pre-surgical planning and generally superior to simple flashed checkerboards or pulsed lights (DeYoe et al., 2011). It is also time efficient in that all eccentricities or polar angles throughout the visual field can be mapped in less than 4 minutes.

As illustrated in Figure 3 A, B, the fMRI signals produced by temporal phase mapping are periodic waveforms that are distinguished from each other by their temporal phases. As the wedge/ring sweeps through each visual field location, fMRI activation sweeps through retinotopically corresponding locations in visual cortex. The timing of the activation at a particular brain voxel is determined by the distance of a voxel's "population receptive field" (pRF) (Dumoulin and Wandell, 2008) from the stimulus onset location plus a delay due to the sluggish hemodynamic mechanism responsible for the fMRI signal. Consequently, the ability to precisely locate the pRF of a given voxel is limited by the accuracy of the estimation of the temporal properties of the signal and the variability of the local hemodynamics. Computing the temporal phase of the fMRI signal is typically accomplished by cross-correlation with a reference waveform (e.g. sinusoid) (Bandettini et al., 1993; Saad et al., 2003) or through Fourier analysis (Boynton et al., 1996; Engel et al., 1997). Removing the additional phase delay caused by the BOLD hemodynamics can be achieved with fMRI scans using stimulus moving in opposite directions, such as clockwise versus counterclockwise rotating wedges or expanding versus contracting rings (Serenio et al., 1995). For each voxel, the phases obtained with stimulus moving in opposite directions can be averaged to cancel out the phase shift caused by the delay of hemodynamics. Then the time series, corrected for this phase

shift, acquired with stimulus moving in opposite directions can be averaged for improved SNR.

The dependence of temporal phase mapping on precise timing of the fMRI signal makes it susceptible to random signal distortions. Though correlation methods used with temporal phase mapping can provide good immunity to some types of pulse or burst noise, other types of noise can blur the small phase difference between responses evoked by adjacent visual field locations, thus introducing errors in preferred stimulus location. In addition, if a voxel contains a mixture of neurons with spatially distinct receptive fields, as can occur for a voxel straddling a sulcus, then the voxel's response will be a sum of multiple (approximate) sinusoids having the same period but different phases. A sum of pure sinusoids is, if non-zero, a single sinusoid with an erroneous phase intermediate between those of the components. As a result, the estimated preferred stimulus location for that voxel will also be in error. Similar problems can plague any mapping method that is fundamentally dependent on the precise phase of a periodic fMRI signal. This is true of typical stimuli (drifting bars) and analyses used to model population receptive fields (Dumoulin and Wandell, 2008; Smith et al., 2001).

While the susceptibility of such methods to temporal distortions can be controlled in studies with healthy subjects by ways of averaging time series from multiple , this is not necessarily the case for clinical applications in which rapid, reliable mapping must be accomplished in the presence of brain pathologies that may exacerbate these factors. In sum, mapping methods dependent on precise fMRI response timing may not be optimal for clinical use.

Random multifocal mapping

A potential solution to the problem of temporal distortion is to use a code-based mapping paradigm such as randomized multifocal stimulation. Figures 3 C-E illustrate

multifocal visual stimuli consisting of multiple checkered segments that are each presented in a unique randomized temporal pattern. Multifocal stimulus paradigms have been used to explore visual cortex using a variety of neurophysiological techniques including visual evoked potentials (VEP) (Baseler et al., 1994; Slotnick et al., 1999), magnetoencephalography (MEG) (Tabuchi et al., 2002), and fMRI (Hansen et al., 2004; Vanni et al., 2005). In this approach, the stimulus segments to which a voxel responds best can be identified by the unique ON/OFF pattern of the fMRI response. In other words, each stimulus sequence can be viewed as a unique temporal code for a specific region of the visual field. To identify which stimulus segments activate a particular voxel, a conventional multiple regression analysis can be employed with the unique time series of each stimulus segment used as a regressor (Ward, 2006).

The multifocal mapping technique has showed its potential in clinical applications, including post-surgical examination of the primary visual cortex (Vuori et al., 2012), and revealing of training-induced cortical representation of a hemianopic hemifield (Henriksson et al., 2007). It was also suggested that the time multifocal mapping saves compared to isolated static stimuli might be beneficial for scanning elderly glaucoma patients (Duncan et al., 2007b). One advantage of this approach is that a voxel's response may be found to consist of multiple components evoked by adjacent or even separate stimulus segments thereby correctly identifying voxels having extended or spatially complex pRFs. Also the unique ON/OFF 'digital code' associated with each stimulus segment potentially makes the analysis more tolerant of temporal distortions. Indeed, computational simulations indicate that a random stimulus paradigm does provide better immunity to noise and hemodynamic variations, and thereby increases the accuracy of identifying the specific stimulus locations to which a voxel responds (Ward et al., 2012).

In this paper we describe a randomized multifocal mapping technique that permits more flexible presentation sequences than popular maximum-length-shift-register sequences (m-sequences) (Buracas and Boynton, 2002; Sutter, 2001), and compare it with conventional temporal phase mapping on a number of clinically relevant measures including effectiveness, efficiency and noise immunity. The use of more flexible presentation sequences permits greater control over scan duration, which can be advantageous for clinical applications. This includes real-time brain mapping paradigms in which scan length is adjusted adaptively based on recursive estimation of data quality (Ward et al., 2012).

Material and methods

Subjects

Seven subjects (three female), 18-35 years old, participated in this study. All subjects had normal or corrected-to-normal visual acuity and provided informed, written consent in accordance with methods approved by the Institutional Review Boards of both the Medical College of Wisconsin and Marquette University.

Visual stimulation

The randomized multifocal stimulus (Figure 3 C-E) consisted of an array of segments arranged in concentric rings so that each segment covered a predetermined range of eccentricity and polar angle thereby allowing both dimensions to be mapped simultaneously. As shown in Figure 3 C-E, we tested three randomized stimulus patterns consisting of 13 (3 rings x 4 wedges + 1 center segment), 25 (3 rings x 8 wedges + 1

center segment), and 49 segments (3 rings x 16 wedges + 1 center segment). The 3 rings of segments extended radially from 0.32° to 20° visual angle, with borders at eccentricities of 3.2° and 8.55° visual angle. The rings were scaled in size based on the retino-cortical mapping function reported by Schira et al. (Schira et al., 2010; Schira et al., 2007), so as to stimulate roughly comparable-sized patches of primary visual cortex.

Figure 3 also shows single 2 sec. stimulus frames and stimulus timing waveforms for 3 locations in the visual field. For the random stimuli, individual segments were turned ON and OFF during the fMRI scan using unique, 600 sec., random presentation sequences, three of which illustrated at the right of Figure 3. Typically, one unique set of random sequences were used twice with each subject and the resulting fMRI time series were concatenated to provide a single 1200 sec. series. Within each stimulus sequence, ON block durations varied from a minimum of 10 sec. to 40 sec. and intervening OFF blocks varied from 2 to 88 sec. while maintaining either a 25% or 50% duty cycle overall depending on the experiment. Specific sets of sequences were selected from 1000 randomly generated sets so as to minimize the error in estimating the fMRI response attributable to each stimulus segment, in other words, to maximize estimation accuracy. Specifically, a covariance matrix was calculated for each set of random stimulation sequences after convolution with a standard hemodynamic response function (Cohen, 1997). The covariance matrices were then compared to identify one stimulus set with the smallest, maximum covariance.

For comparison, we used conventional temporal phase mapping stimuli consisting of an expanding ring or rotating wedge (Figure 3A, B). To map visual field eccentricity from 0.4° to 20° radius, this range was divided into 16 elementary rings scaled according to the formula $R_{\min} = R_{\max} * f^N$, where R_{\min} / R_{\max} was the innermost/outermost radius- 0.4°/20° (vis. ang.) and N was the number of the

elementary rings. At the beginning of each run, the stimulus consisted of just the center segment (area within 0.4°) and then recruited one more elementary ring each 2 sec. until the center segment plus 3 elementary rings were included. Then the combined ring shifted outward by one elementary ring every 2 sec. until it slowly disappeared in steps at the outer margin of the display. The display was uniform gray for 2 sec. then the sequence repeated from the center. Each full cycle contained 20 steps (40 sec.), and each scan had 20 cycles, thus spanned a total of 800 sec. To map polar angle, a checkered wedge spanning a quarter of the visual field rotated counter-clockwise in 20 steps (40 sec.) beginning centered on the lower vertical meridian. The rotation of the wedge was also repeated 20 times per scan for a total of 800 sec.

Regression analysis of random mapping data

For the random mapping data, linear regression was used to detect activated voxels and determine the stimulus segments to which they responded. Given that the hemodynamic delay across visual areas varies for 0.46 seconds at most (Puckett et al., 2013) and thus is unlikely to cause any significant difference in the timing of the random signals from different visual areas, an finite impulse response (FIR) analysis where is not necessary. This was accomplished using AFNI's 3dDeconvolve (Cox, 1996a; Ward, 2006), which performs multiple linear regression using multiple input stimulus time series. In the multiple linear regression model for random mapping data, regressors consisted of the individual time series for each stimulus segment convolved with the default AFNI HRF. The default HRF was a gamma variate function $HRF(t) =$

$$t^{86} * e^{-t/0.547} \text{ (Cohen, 1997), where } t \text{ represents time in seconds. A nuisance}$$

regressor consisting of a 3rd order polynomial was also included, to model baseline drift.

The regression analysis generated a least squares estimate of the fit coefficients and a partial F-statistic for each voxel with respect to each random segment's regressor. The goodness of fit for the whole model with all regressors was quantified by a full F-statistic. For each voxel, the random stimulus segment with the largest partial F-statistic was recorded as the 'best segment' for that voxel and the ring and wedge comprising this segment were recorded as 'best ring' and 'best wedge'. Both the full and largest partial F-statistics for each voxel were converted to z-scores having equivalent statistical p-values to facilitate comparison with the temporal phase mapping results.

Correlation analysis of phase mapping data

The fMRI responses generated by phase mapping were evaluated using the Hilbert Delay function (Saad et al., 2001) of the AFNI package. This function yielded the maximum cross-correlation between each voxel's BOLD response and a reference sinusoidal waveform, and provided the optimal time lag at the point of maximum cross-correlation. The correlation coefficient at the optimal time lag of each voxel was converted to a z-score having the same p-value as the original correlation coefficient.

As mentioned in the introduction, the temporal phase shift of a voxel's BOLD response is determined by its preferred location in the visual field plus an additional phase shift caused by the hemodynamics. Phase shifts for all activated voxels were corrected to account for this hemodynamic component prior to determining the preferred stimulus location for each voxel. To make this correction, the FMap calibration process described in Chapter 2 was performed by trained personnel.

Visual area delineation

To view retinotopic maps, a 3D cortical surface model of each subject's hemisphere was reconstructed from the high resolution anatomical data using Caret software (Van Essen et al., 2001), as shown in Figure 4A. The surface model was then computationally unfolded to yield a 2D flat map of the cortex (Figure 4B).

FMRI time courses were spatially filtered by a 3.5mm averaging kernel to make more coherent retinotopic maps. Maps made from both filtered and unfiltered time series are displayed in Figure 5. FMRI data used in all other analyses were not filtered spatially or temporally.

ROIs of visual areas were delineated based on consensus of two raters through visual inspection of the phase-encoded retinotopic maps. Specifically, the flat maps were first colored by voxels' phase shifts from polar angle mapping. Boundaries were drawn at the place where the sequential color pattern reversed itself, which indicated a phase reversal. Boundary of each visual area was closed to include a complete hemi or quarter field representation, and cross checked with eccentricity phase maps to ensure that each visual area contained a foveal representation. Depending on the quality of the retinotopy for each subject, up to nine complete visual areas, V1, V2, V3, V3AB, hV4, hMT+, V7, VO1, VO2, were identified using published criteria (Arcaro et al., 2009; Hansen et al., 2007; Harvey and Dumoulin, 2011; Swisher et al., 2007; Wandell et al., 2007; Winawer et al., 2010). A set of these 9 areas for one subject is shown as colored patches on the cortical surface models in Figure 4. In the worst case, three complete visual areas and five half visual areas (only one hemisphere) were identified.

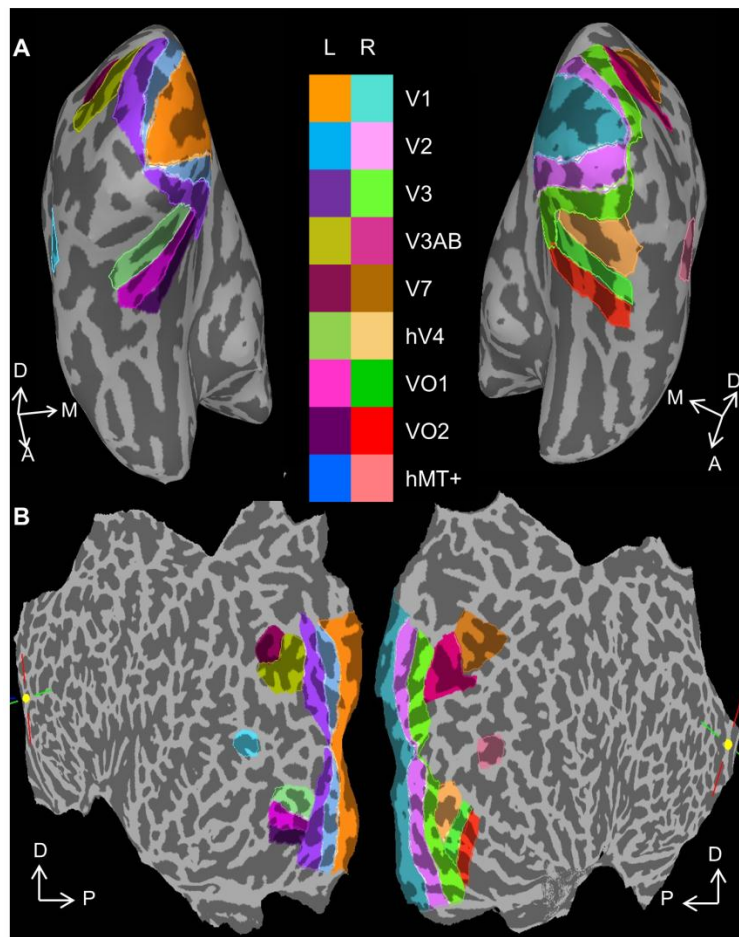


Figure 4. Visual area ROIs. A. 3D cortical surface models with legend indicating colors assigned to different visual areas. B. 2D flat maps of the two hemispheres of one subject. D: Dorsal, M: Medial, A: Anterior, P: Posterior. Visual area names according to Swisher et al., 2007, Arcaro et al., 2009.

Effects of noise

To test the effect of noise on the ability to correctly classify each voxel's responding location of phase and random mapping, we simulated two new experiments with 20 stimulating wedges throughout the visual field under two assumptions for fMRI signal: BOLD signal is linear (Boynton et al., 1996; Hansen et al., 2004) and the noise is white. Although fMRI response can be non-linear under certain conditions, it is

reasonably linear as long as the stimulation duration is longer than about 4 seconds (Gu et al., 2005), which is true for most retinotopic mapping experiments. It is known that non-white noise is present in BOLD signal (Lund et al., 2006). However, these differences will likely be quantitative rather than qualitative. The goal of our analysis was to demonstrate that there was a qualitative difference in how noise affects the retinotopic classification of phase and random mapping.

To demonstrate the differential effects of noise on the two techniques, we wanted all conditions to be constant other than the addition of noise. This can be accomplished most precisely in the context of a pure simulation. For the simulated phase mapping, the 20 wedges were turned ON/OFF using periodic sequences cyclically shifted in time, simulating the temporal stimulating sequences of phase mapping. For the simulated random mapping, the 20 wedges were turned ON/OFF using random sequences, replicating the temporal stimulating sequences of random multifocal mapping.

The ON/OFF sequence from one wedge was used to simulate 100 fMRI time series at an SNR of 5 and 0.5. To do this the selected ON/OFF sequence was convolved with an estimate of the hemodynamic response function. Next, 100 series of normally distributed pseudorandom numbers generated by the “randn” function of MATLAB were scaled to a power determined by the desired SNR and added to the sequence generated in the previous step. Finally, the same regression analysis used to analyze the empirical data was used to analyze the simulated time series. The 20 random ON/OFF sequences associated with the stimulus wedges were regressors. From the regression analysis, the wedge whose ON/OFF sequence best matched each simulated time series was identified. A histogram of the number of simulated time series that were assigned to each wedge was then constructed.

For phase mapping, 20 phase-shifted periodic square waves having the same

length as the sequences for random wedges and a period of 40 sec were used to simulate the ON/OFF sequences associated with the 20 wedge locations. One hundred fMRI time series were then simulated in the same way as for the random mapping. The same correlation analysis used to analyze the empirical phase-based fMRI data was used to analyze the simulated time series. The resulting delay values were grouped into 2 sec bins to generate an equivalent histogram to that prepared for random mapping. For both paradigms at both SNR levels, the response measures (F-statistic, correlation coefficient) were thresholded at an equivalent p-value (7.1×10^{-5}) to identify significant responses included in the histogram.

Effects of duty cycle

Duty cycle is an important design parameter for random multifocal stimulation because it controls the number of segments that, on average, are ON or OFF at the same time, which subsequently determines the amount of modulation for a voxel that is stimulated by more than one segment. Therefore we also performed an experiment comparing random 25-segment multifocal mapping with 50% duty cycle, 25% duty cycle and with the phase-mapped polar angle mapping, which produces a 25% duty cycle as described above in section 2.2. Data acquisition and analysis followed the procedures described in section 2.2-2.5. This experiment was performed with two subjects.

Stability of eye fixation

Stable and accurate eye fixation ensures the targeted stimulation of the retina by our stimulation paradigm, thus plays an important role in retinotopic mapping, especially in clinical context where larger variations in eye positions might be present from various

pathologies. It may be expected that the random, unpredictable form of the multifocal stimuli would facilitate accurate fixation relative to the phase-mapping approach.

Therefore, we performed an eye tracking experiment outside the scanner with the subject whose retinotopic maps are shown in Figure 5.

The subject was asked to keep his head as still as possible and maintain fixation on the central green marker. A bite bar customized for this subject was used to keep a steady head position. We presented random 25-segment stimuli, expanding ring stimuli and rotating wedge stimuli in three separate runs while tracking the eye position of the subject. Each run was 616 seconds to match the run length inside the scanner as close as possible (expanding ring and rotating wedge runs inside the scanner were 816 seconds, which are too long for the subject to stay on the bite bar). The luminance levels for black and white color were 0.89 cd/m² and 115 cd/m², resulting a contrast of 98%. Eye position was tracked at 250 Hz with an eye tracker (Eyelink II, SR Research Ltd., Mississauga, Ontario, Canada). The Eyelink II system has two eye cameras, mounted on a comfortable padded headband, tracking the pupil position. Calibration and drift correction were performed at the start of each run. The Eyelink II system incorporates a unique on-line parsing system that analyzes eye position data into meaningful events (saccades, fixations and blinks). For each data sample, the parser computes instantaneous velocity and acceleration. If either the velocity is above 30 degrees/second or the acceleration is above 8000 degrees/second², a saccade is detected (Ltd).

The subsequent processing is performed on these identified fixation events after a linear trend was removed. Specifically, a bivariate contour ellipse area (BCEA) was calculated for each run using the formula $BCEA = 2k\pi\delta_h\delta_v(1 - \rho^2)^{1/2}$. δ_h and δ_v are weighted std. dev. along horizontal and vertical axes, ρ is weighted correlation

coefficient, and k is set to 1.14 to encompass 68% of the fixation events. The duration at a location was used as the weight for that location.

Results

We compared random multifocal mapping and temporal phase mapping with respect to effectiveness in rendering retinotopy, as well as time efficiency and noise immunity that are of particular relevance for clinical use. We also explored the effect of duty cycle on random multifocal mapping.

Effectiveness

- *Rendition of retinotopic features*

In a clinical context, retinotopic maps assist the physician in understanding the relationship between the functional organization of visual cortex and the integrity of visual perception across the patient's visual field. As illustrated in the top half of Figure 5 for one subject, both phase mapping and random mapping generated clear retinotopic maps within V1, V2 and V3 (outer boundary of V3 is marked by white curve). Retinotopic maps for extrastriate areas beyond V3 were more homogeneous for phase mapping than for random mapping. Phase mapping revealed at least 6 more visual areas including V3AB, hV4, V7, VO1, VO2, hMT+. This trend was evident in all 5 subjects. The global features of all retinotopic maps were accentuated by spatial filtering of the volumetric time course data with a spherical averaging kernel of 3.5 mm radius, as shown in the bottom half of Figure 5, though this is at the expense of some loss of local detail, and the potential introduction of retinotopic distortions (e.g. compare the unfiltered

vs filtered polar angle maps for area MT in the left hemisphere)¹. Even with smoothing, the extrastriate retinotopic map obtained with random stimulation still appears less homogeneous than for phase-mapping.

¹The use of spatial smoothing of volumetric time series data is so prevalent in the literature as to effectively be standard operating procedure despite the potential problems it can cause for a variety of quantitative analyses.

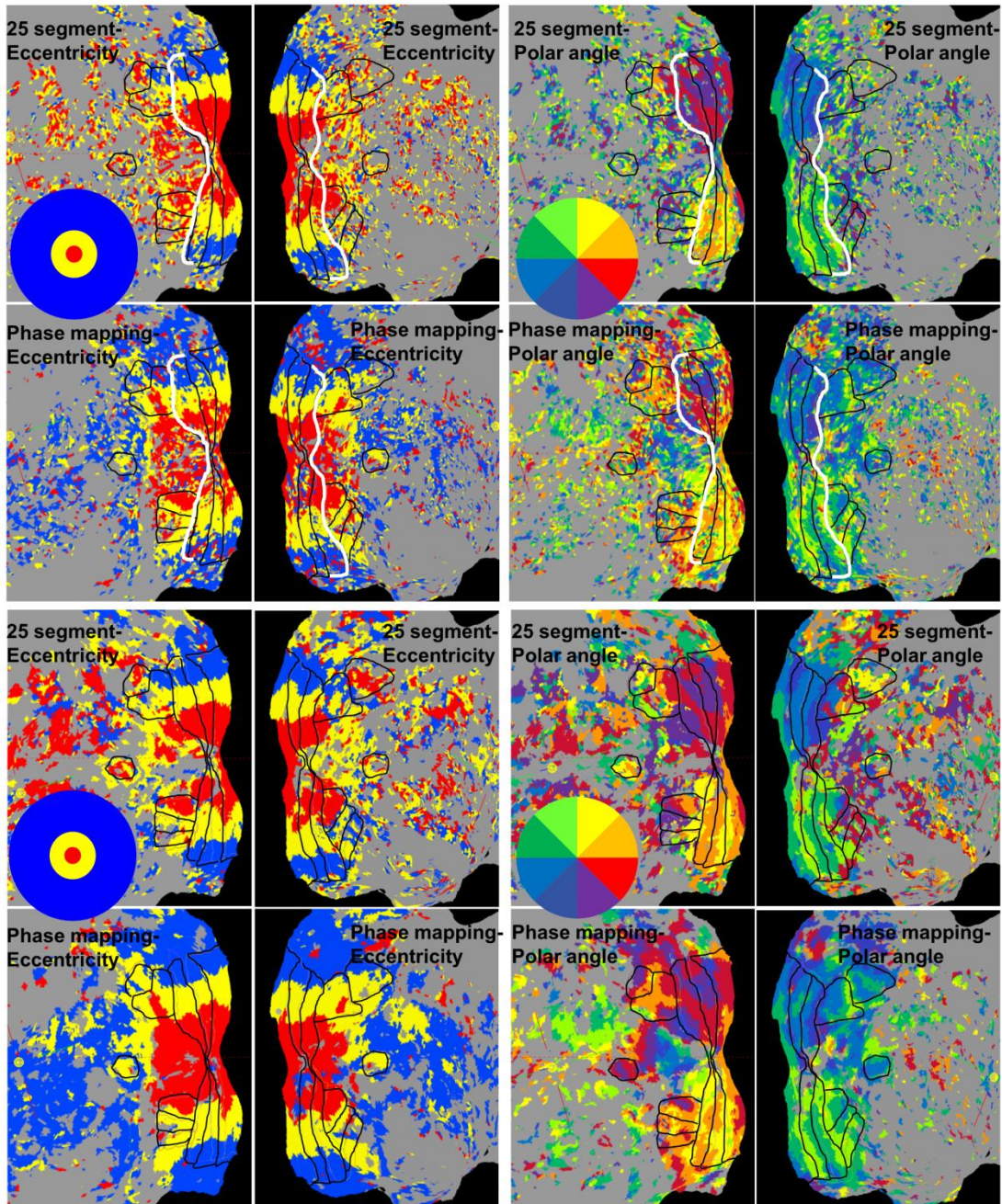


Figure 5. Retinotopic maps from one subject on flat brain surfaces. Black outlines: Visual area boundaries as defined in Figure 2. White curve: border between V3 and higher visual areas. Top: Maps without spatial or temporal smoothing. Bottom: Maps after a spatial smoothing with a 3.5 mm spherical kernel applied to volumetric fMRI time series data.

- *Consistency of voxel based retinotopy*

Overall, random and phase-mapping tend to yield comparable retinotopic assignments for each voxel in V1-V3. This can be appreciated qualitatively by noting the general similarity of the retinotopic maps within V1-V3 in Figure 5. To assess this quantitatively, we first identified groups of voxels that responded most strongly to each of the different random stimulus segments. We pooled voxel groups preferring segments at the same polar angle. For each pooled group, we then constructed a histogram of the preferred phase mapped angles. Figure 6A shows the histograms for each pooled group with the angular range of the corresponding random mapping segments marked by the shading in the background. (All histograms shown in Figure 6 were averaged across five subjects.) This analysis was not conducted in visual areas beyond V3 based on the retinotopic maps in Figure 5 and z-score analysis shown in Figure 8 (details presented in section “Efficiency”), which showed that random multifocal mapping did not evoke meaningful responses in visual areas beyond V3. Note that in V1, each phase mapped histogram is roughly symmetrical and overlaps the range of angles spanned by the corresponding group of random stimulus segments, thereby indicating good consistency between the random and phase-mapping retinotopic assignments. The uneven heights of the histograms reflect differences in the number of voxels representing each angular location consistent with other reports from this lab (Janik et al., 2003). In V2 and V3, the correspondence between each histogram and each background shading was conserved roughly, with random rightward or leftward shift of some histogram peaks, indicating a degrade in the consistency of retinotopic assignments between random and phase mapping going up the hierarchy of cortical visual system.

Figure 6B shows the average of the individual histograms in 6A after magnitude normalization and shifting to a common center. The shading in Figure 6B shows the 45 degree range ($\pm 22.5^\circ$) that is spanned by each group of random mapping segments at

the same polar angle. It is evident that a single random mapping wedge preferentially activates voxels whose preferred phase-mapped angle extends beyond the range spanned by the segment itself. The extents of this “over-activation” are similar in V1, V2 and V3, indicated by the similar widths of the three normalized and averaged histograms.

The same approach was used to create the eccentricity-related histograms of Figure 6C. Here the widths of the three histograms in each graph appear to vary because the eccentricity ranges of the corresponding random rings vary with eccentricity in order to roughly compensate for changes in cortical magnification with eccentricity. It is also obvious that the phase-mapped histogram peaks are skewed toward greater eccentricities relative to the corresponding random stimulus rings. This effect appears particularly pronounced in Figure 6C, partly due to the non-linear scaling of the stimulus rings but also may reflect some bias in the calibration of the temporal phase data.

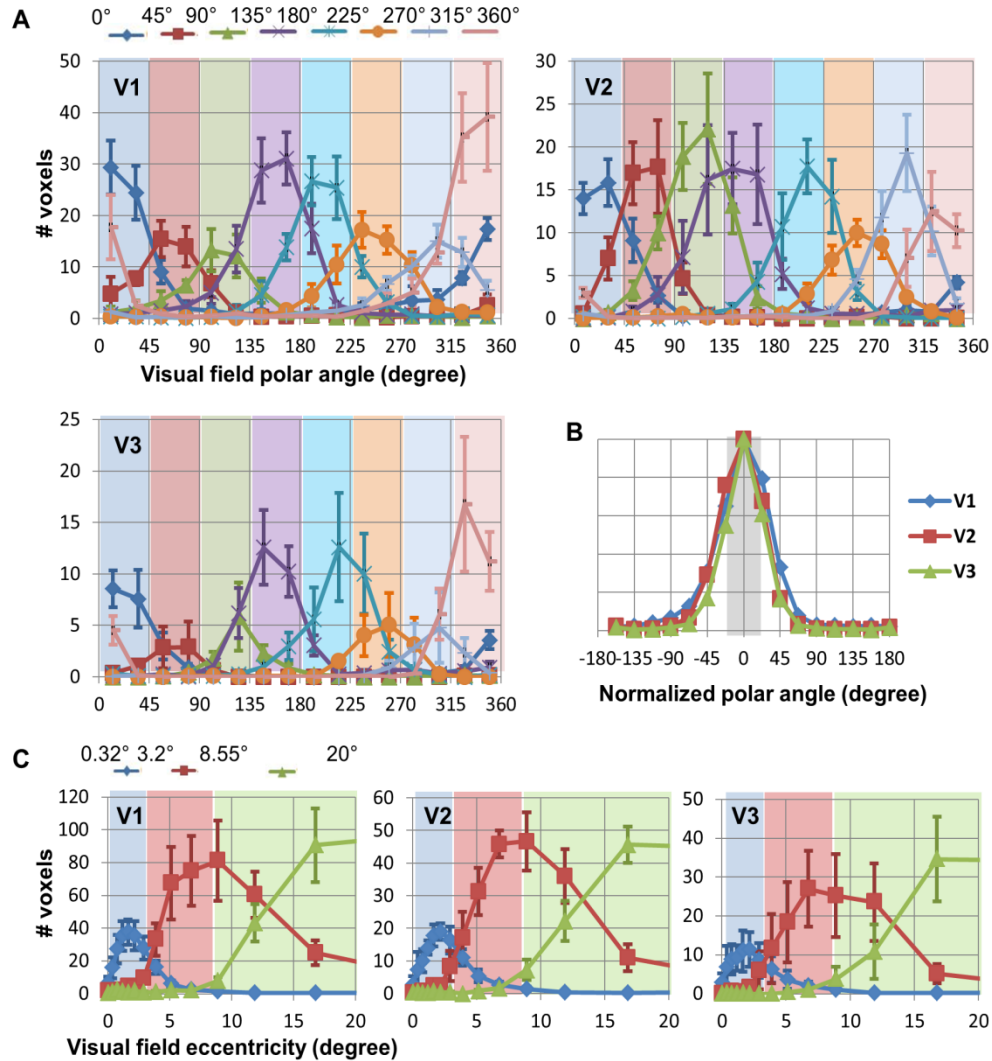


Figure 6. Correspondence of retinotopic assignments in V1, V2 and V3 between phase and random mapping. A. Correspondence between preferred polar angle for phase mapping (line graphs) and preferred random wedge (color shading). Averaged for five subjects. B. Average phase mapped, polar angle distribution (line graph) vs. width of a single random wedge (gray shading). C. Correspondence between preferred eccentricity for phase-mapping (line graphs) and preferred random ring. NOTE: Ring widths were scaled in proportion to eccentricity.

- *Non-uniform representation of visual field locations*

Previously, we have shown that temporal phase-based retinotopic maps of V1

often show a significant under-representation of voxels responding preferentially to visual field locations near the vertical meridian as compared to the horizontal meridian (Janik et al., 2003). In this study we revisited this issue using both phase and random mapping. For both methods, the numbers of voxels responding best to different polar angle locations were non-uniform for V1 but less so for V2 and V3 (Figure 7, averaged for five subjects). More voxels represented the horizontal meridians than the vertical meridian (note color code in Figure 7).

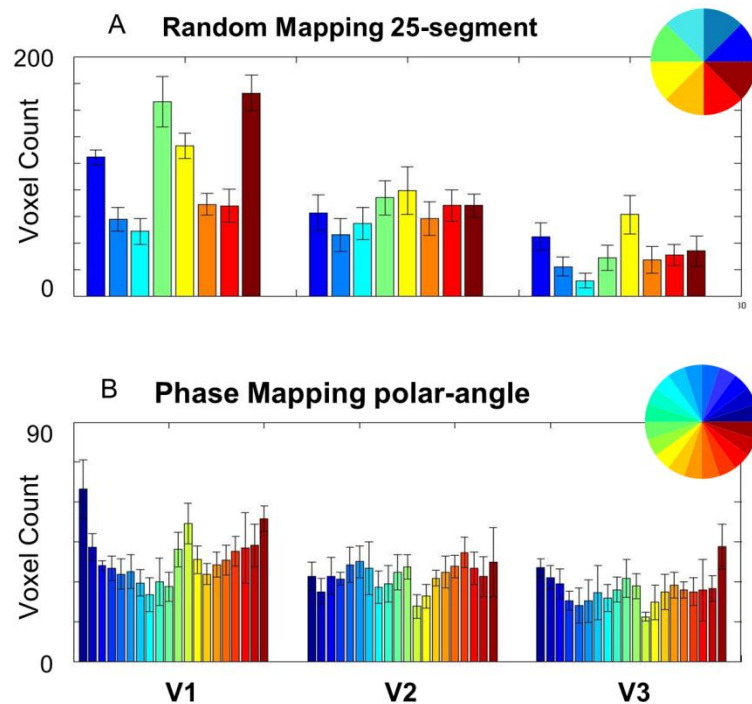


Figure 7. Number of voxels having different preferred polar angles for (A) random mapping and (B) phase mapping. Averaged for five subjects. Inset: Color code for preferred angle.

Efficiency

For clinical patients who may have attention, alertness or cognitive difficulties, time efficiency can be a critical factor in determining the success or failure of an fMRI exam. Consequently, we inspected the efficiency of the two mapping paradigms with respect to the duration of data acquisition needed to: 1) determine the responsiveness/non-responsiveness of each voxel and 2) stabilize the number of voxels responding to each stimulus location.

- *Responsiveness of visual areas*

For the random mapping paradigm, the F-statistic for the full regression model provides an overall indicator of a voxel's ability to respond significantly to one or more of the stimulus segments. The temporal correlation coefficient provides an analogous statistic for phase mapping. (A regression model cannot be used for phase mapping due to multicollinearity of its design matrix comprising phase-shifted sinusoidal sequences as column vectors.) To permit a quantitative comparison between the F- and correlation statistics, we converted both to equivalent z-scores. Figure 8A shows the mean and the upper and lower quartiles of the z-scores for all voxels within each cortical visual area averaged across five subjects as a function of data acquisition time for phase-mapped polar angle mapping and random 25-segment mapping. Curves for polar angle mapping are colored black while those for random 25-segment mapping are colored red. In all visual areas, the z-scores for polar angle mapping increased faster with acquisition time than those for random mapping. In other words, polar angle mapping was more efficient with respect to the data acquisition time needed to achieve a specified level of statistical significance. This was confirmed by a 3-way ANOVA that showed significant main effects

($p < 0.05$) for mapping method (random vs polar angle), acquisition time and visual area as well as significant interaction effects ($p < 0.05$) for method vs. acquisition time.

(Interaction tests were only computed using data at time points common to both polar angle and random mapping, i.e. 200, 300 and 400 sec.) Other interaction effects were not significant. The graphs of Figure 8A also show that random mapping was not capable of strongly activating visual areas other than V1, V2, and V3 even at the longest scan duration of 1200 sec. This is consistent with the qualitative impression obtained from the cortical maps in Figure 5. One thing to note is that the phase-mapped eccentricity mapping was always more efficient than polar angle mapping (data not shown).

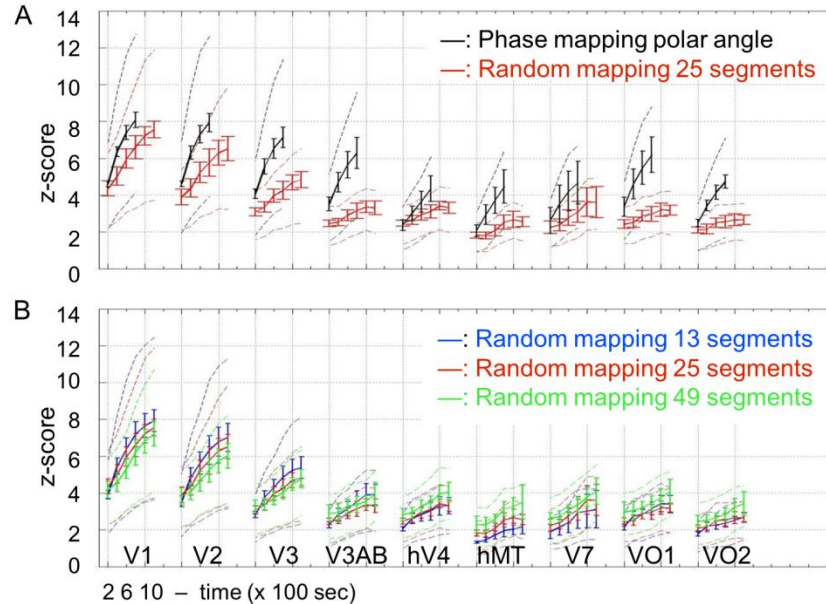


Figure 8. Time efficiency represented by z-scores. A. Time efficiency for random vs phase mapping in different visual areas. B. Time efficiency for random stimuli with 13, 25 or 49 segments. Solid lines: mean z-score. Error bar = standard error of the mean. Broken lines: Lower and upper quartiles.

Figure 8B shows the averaged mean and upper and lower quartiles as a function of acquisition time for random mapping with different numbers of stimulus segments (13, 25, and 49). ANOVA showed significant main effects ($p > 0.05$) for number of stimulus segments, acquisition time and visual area as well as significant interaction effects between all three pairs of factors. It is also noteworthy that in V1-V3, z-scores improved slightly faster (steeper slope) for smaller numbers of segments. In visual areas beyond V3, z-scores didn't increase much for any number of segments, but they tended to be higher for larger rather than smaller numbers of segments.

We repeated this same analysis using the largest partial F-statistic for each voxel rather than the full F but obtained virtually identical results suggesting that for the vast majority of voxels the response may be primarily driven by a single random segment. Since both our qualitative and quantitative assessments indicated that random mapping as performed here was not effective beyond V3 for all five subjects, all subsequent comparisons focus on data just from V1-V3.

- *Stabilization of retinotopic assignment*

Another measure of fMRI mapping efficiency is the time needed to reach a stable assignment of retinotopic preference for each voxel. This measure goes beyond simply identifying a voxel as responsive to determining the specific retinotopic locations that contribute to its response. To assess this factor, we tracked the number of voxels²

² We used fractional voxel counts for random mapping since a voxel could respond to more than one random segment. In these cases, the fraction of a voxel contributing to a particular

responding to each stimulus location (random segment or phase-mapped polar angle location) as a function of data acquisition time. In Figure 9A and 9B the top rows of graphs show the increase in the total number of voxels identified as responsive in visual areas V1-V3 versus data acquisition duration. Graphs in the second rows track the number of voxels responding preferentially to each of the 25 stimulus segments or the 20 phase-mapped polar angle positions (Each segment or position is represented by a different colored line). Finally, the third rows of graphs depict rate-of-change (1st derivative) of the voxel counts. We defined the time-to-stabilize as the time point when the mean unsigned rate-of-change first fell below 20% of the peak rate-of-change (Figure 9, red, blue dashed lines). In panel A, the graphs show that for random mapping the numbers of voxels responding to each stimulus segment tend to stabilize within approximately 300 sec. for V1, 360 sec. for V2, and 510 sec. for V3. However, the ‘settling’ behavior for phase-mapped polar angle mapping is noticeably different, as shown in panel B. The total number of voxels identified as active is almost constant after the first one and half cycles of stimulus presentation (60 sec.). But, the numbers of voxels preferring each polar angle position vary widely during the first 120 sec. for all three visual areas. On the whole, voxel counts for phase-mapped polar angle mapping were less stable than for random mapping as best appreciated in the rate of change graphs. After stabilization, the mean unsigned rate-of-change was 4 times larger for polar angle mapping compared to random mapping.

segment was computed by dividing the voxel’s regression coefficient for the individual segment by the sum of the coefficients for all segments that evoked significant responses from that voxel. Thus, the sum of the fractional counts for each voxel summed to 1.0.

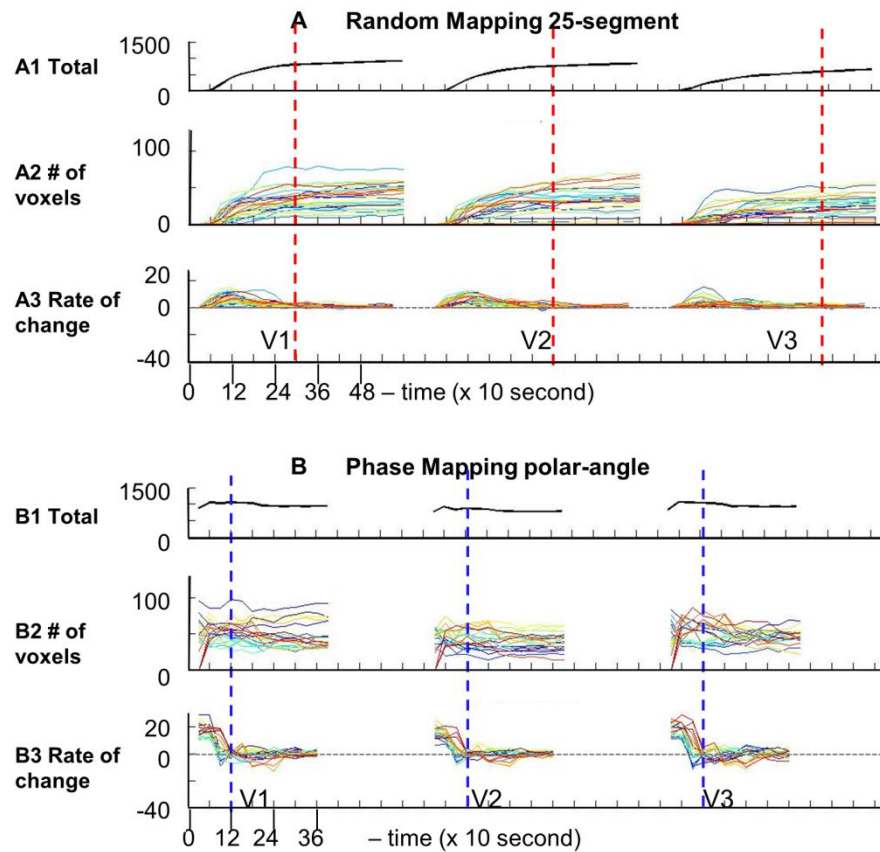


Figure 9. Time evolution of voxel activation for (A) Random vs (B) Phase mapping in visual areas V1,V2,V3. A1,B1: Total number of activated voxels for all visual field locations. A2,A3: Number of activated voxels for each individual visual field location (separate curve for each). A3,B3: Rate of change of voxel counts for each stimulus location (separate curve for each). Dotted lines: Stabilization times.

Effects of noise

The retinotopic assignments of 100 simulated time series by random and phase-based paradigms under two different SNR levels are shown as histograms in Figure 10. When SNR=5, all simulated time series passed the statistical threshold of $p < 7.108e-05$ and were correctly assigned to the stimulating wedge by both paradigms. When SNR=0.5, phase mapping mis-assigned 23% of time series to the neighboring wedges even though all 100 time series passed the same threshold. However, a small number of

incorrect, but neighboring assignments do not cause any practical problem currently, although conceptually they might shrink or enlarge a representation of a scotoma. Importantly, for random mapping, the addition of random noise does not cause the time series to be assigned to an incorrect location. Rather, 5% of the time series merely fail to reach statistical significance thus ‘drop out’ of the analysis. Note that this simulation was under two assumptions for fMRI signals: BOLD signal is linear and the noise is white.

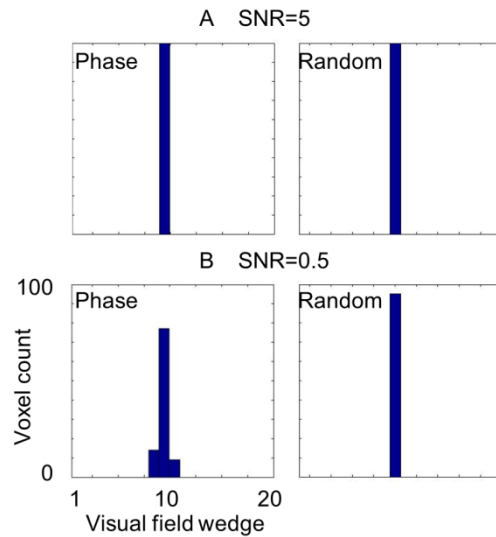


Figure 10. Effect of noise on preferred wedge location for simulated random and phase mapped responses to a single wedge location (#10). Histograms include only responses that are statistically significant ($p < 7.108e-05$) A. SNR=5. B. SNR=0.5.

Effect of duty cycle of the random stimulation sequences

Figure 11 illustrates the effect of duty cycle on the z-scores of random multifocal mapping averaged across two subjects. In V1, Z-scores of random multifocal mapping with a 25% duty cycle (blue curve) increase slightly faster than for a 50% duty cycle (red

curve). This difference was increasingly apparent in V2, V3, V3AB, and hV4. However, phase-mapped polar angle mapping was still more efficient than random mapping at either duty cycle. A 3-way ANOVA showed significant effects ($p < 0.05$) for method (25% duty cycle, 50% duty cycle, and phase), visual area and acquisition time. Interaction effects between all three pairs of factors were also significant ($p < 0.05$).

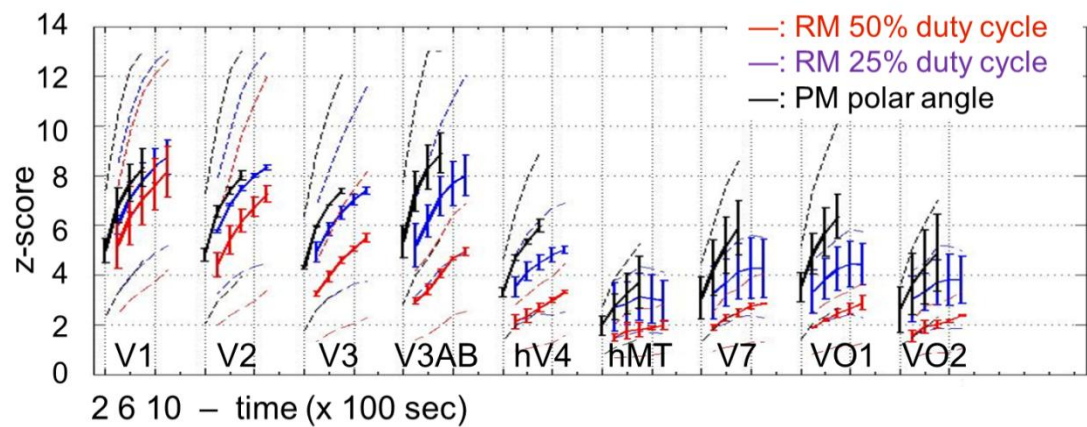


Figure 11. Effect of duty cycle on time efficiency of random stimulation across visual areas. Solid lines: Mean z-score. Error bar = standard error of the mean. Broken lines: Lower and upper quartiles. Polar angle phase mapped curves shown for reference.

Stability of eye fixation

The subject whose eye fixations were monitored outside the scanner showed small fixation scattering. Figure 12 shows the scattering of fixations relative to the sizes of the fMRI mapping stimuli represented by the solid black outlines. However, to appreciate the true scatter we have enlarged the central 3.3 degrees in the insets to each figure and shown standard BCEA (Bivariate Contour Ellipse Area) ellipses (red outlines in insets) which encompass 68% of the weighted fixation positions. The

weighted standard deviations (minutes of arc) corresponding to the horizontal and vertical axes of the ellipses, as well as the BCEA values (minutes of arc²) are reported in Table 1. Note that the weighting factor for each fixation locus is the time at which fixation remained at each location.

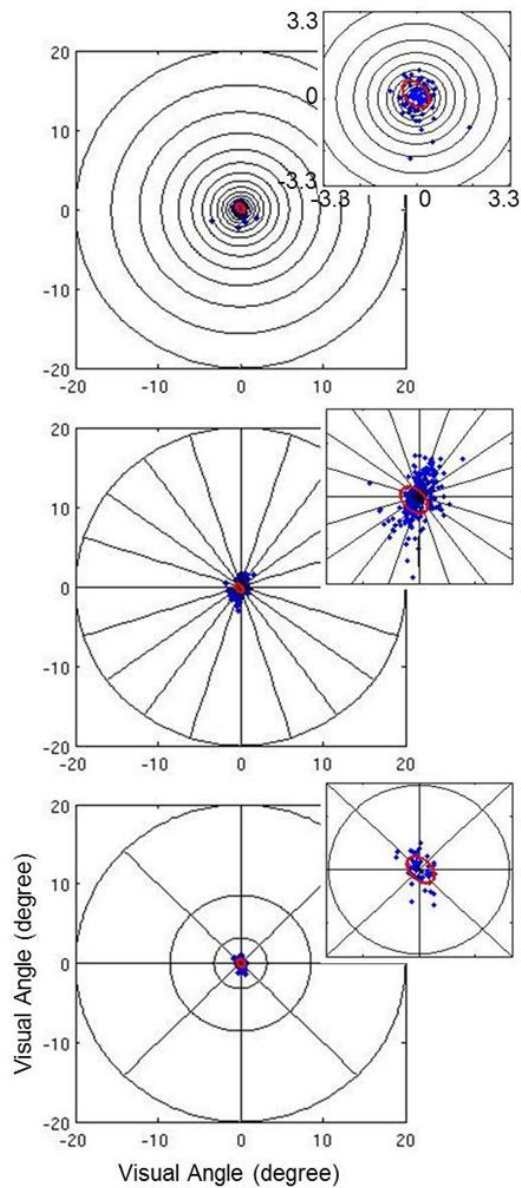


Figure 12. Positions of eye fixations of one subject during visual stimulation. Outlines of

each stimulus are plotted as references. Insets: enlargement of the central 3.3 degrees of each graph.

Eye Position Statistics (min arc/min arc ²)								
Expanding ring			Rotating wedge			25-segment		
δ_h	δ_v	BCEA	δ_h	δ_v	BCEA	δ_h	δ_v	BCEA
17	20	2472	19	41	4562	19	20	2419

Table 1. Weighted standard deviations (δ) horizontally and vertically, and weighted BCEA for each visual field stimulus pattern.

Discussion

We compared random multifocal visual stimulation paradigm with conventional temporal phase mapping. Random multifocal mapping generated good quality retinotopic maps only in V1-V3, while phase mapping rendered retinotopic features in all nine visual areas we delineated. The quantitative analysis of averaged z-scores in each visual area confirmed this observation. Within V1-V3, retinotopic assignments obtained with both methods were consistent for the majority of voxels. Phase mapping was more efficient with respect to both the acquisition time needed to achieve a statistically significant response across voxels, and to achieve stable retinotopic assignments to those voxels, though the asymptotic stability of those assignments was poorer than for random mapping. Decreasing the duty cycle of the random stimuli marginally improved their efficiency, but it still was not as efficient as phase mapping.

Randomized stimulation sequences

Previously m-sequences and quadratic residue sequences have been proposed for fMRI-based visual field mapping (Buracas and Boynton, 2002; Vanni et al., 2005). Mathematically, m-sequences are considered to be maximally efficient (Buracas and Boynton, 2002). However, M-sequences are based on rigid sequence lengths (powers of 2 minus 1) and other constraints that are not necessarily optimal for clinical applications. Therefore, our approach was to use a more flexible method and focus on selecting a unique set of random sequences that maximally reduces the variance of the fit coefficients in our linear regression model, thereby reducing the error in the retinotopic maps. This approach allows the scan length and number of stimulus segments to be flexible, which can then be optimized as most appropriate for a particular clinical application where minimum MR scan time and assurance of scan success may be more important than highly detailed rendition of retinotopic features other than the identification of foveal vision (DeYoe et al., 2011).

Insufficient activation by random mapping

The generally higher z-scores obtained with temporal phase mapping compared to random mapping may reflect an advantage due to the retinotopic organization of visual cortex which may favor focal, spatially sequential stimulation. Perhaps response “recruitment” within relatively large zones of cortex activated by phase mapping stimuli yield enhanced fMRI responses compared to smaller distributed foci of activation evoked by the random multifocal stimuli. Such “recruitment” could be either neural or hemodynamic in origin. In addition, visual attention focused on a single phase mapping wedge or ring may enhance the cortical response compared to random mapping in

which multiple segments spread throughout the visual field provide no consistent target for focal attention. Finally, some extrastriate visual areas might be more sensitive to the “moving” feature of the phase mapping stimuli than static random segments, such as hMT+.

One consistent observation was that random mapping failed to activate extrastriate visual areas beyond V3 that were well activated by temporal phase mapping. This effect may reflect the preference of voxels in higher visual areas toward larger perceptual unit, phase-encoded ring or wedge, rather than a scattering of small segments. It may also be related to the size of the random stimulus segments relative to the sizes of voxel pRFs in different cortical visual areas. Small pRF's such as those in V1 will often be contained entirely or largely within the retinotopic domain of a single random stimulus segment as depicted in Figure 13B (top). As a result the voxel will be fully modulated as the segment turns on and off (Fig 13A middle waveform). In contrast, a voxel in, say, V4 or VO can have a pRF that covers portions of several adjacent stimulus segments as depicted in Figure 13B (bottom). Since each segment is turning ON and OFF randomly, the pRF may rarely be fully stimulated or fully unstimulated thereby leading to poorer modulation as illustrated in Figure 13A (bottom waveform). Note that this effect will be exacerbated as the size of the pRF increases and the size of the stimulus segments becomes smaller. We observed both such effects in our empirical data.

We further explored our conjecture about the effect of pRF size by computationally predicting the fMRI response to our random stimulus using a modified version of the pRF modeling approach described by Dumoulin and Wandell (Dumoulin and Wandell, 2008). Briefly, voxel pRFs were modeled by a 2D Gaussian sensitivity profile but with a range of sizes. The pRFs were then spatially convolved with 2D

“binary” images of our random stimulus. The resulting time series was convolved with an estimate of the HRF (Harvey and Dumoulin, 2011). Finally, “noise” was added to the predicted response waveform in order to achieve a signal-to-noise ratio of 5.0. These simulated fMRI responses were then subjected to the identical analysis procedure used previously for the empirical data. Figure 13B shows a diagram of the random stimulus segments colored to represent the amplitudes of their respective coefficients that optimally fit the simulated response. As one might expect, the more segments the pRF encompassed, the lower was the coefficient for each segment (compare colors in Figure 10B). The full F- statistics also dropped from 28.3966 to 16.4522 as the pRF model increased in size from 2° to 6° vis. ang. Indicative of a poor fit. This simulation supports our interpretation that voxels in higher visual areas with large pRFs are likely to be poorly modulated by the random multifocal stimuli used in this study. We also note that the results from the duty cycle experiment are also consistent with this interpretation in that sequences with a 25% duty cycle could allow better modulation of voxels having pRFs that encompass more than one stimulus segment.

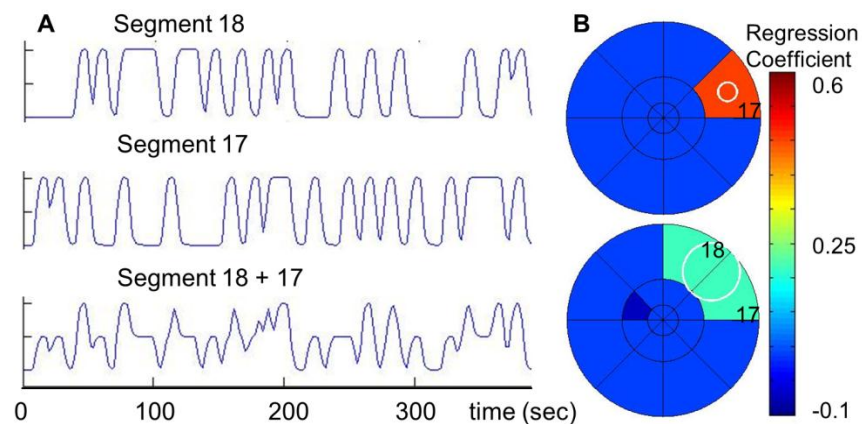


Figure 13. Effect of pRF size on response modulation. A. Simulated pRF responses to segments 17, 18 or both. B. Simulated pRF's (white outlines) relative to random segment stimuli (black outlines) color coded by response magnitude (regression coefficient). Small pRF responds only to segment 17. Large pRF responds to both 17 and 18. Note effect on response modulation.

Time efficiency

Temporal phase mapping proved to be more efficient than the random multifocal mapping paradigm used here on the basis of signal quality versus time (stimulus transitions per unit time). This advantage was compromised, but not eliminated, by the necessity of running the temporal phase mapping paradigm twice to obtain both angular and eccentricity data which are obtained in a single run with the random multifocal stimulation. In addition, to achieve accurate mapping of visual field locations to voxels, temporal phase mapping requires calibration of hemodynamic delays which can vary widely across individuals (Handwerker et al., 2004). Currently accurate calibration requires either additional data acquisition with stimulus pattern moving in the opposite direction, or a time consuming manual calibration process. Although calibration of the hemodynamic delays is not necessary for delineation of visual areas, other potential uses of retinotopic mapping do require calibration (DeYoe et al., 2011). Moreover, calibrated data should be provided if possible, since use of such data in ongoing assessments of a patient clinically might inadvertently assume so. In sum, temporal phase mapping may be more efficient than random mapping in terms of the total time required in most, but not all applications.

The measure of time efficiency used in the study is z-score converted from correlation coefficient and F-statistics. This conversion enabled the direct comparison of phase mapping and random multifocal mapping, but eliminated the meaning of the

original statistics. However, the statistical significance level is kept since the converted z-score has the same p-value as the original statistics. Therefore, z-score suffices as a measure of efficiency in terms of the time needed to achieve a statistical significance level.

Non-uniform representation of visual field locations

For both clinical and academic uses of fMRI an often overlooked issue is whether fMRI maps are “functionally complete”. For visual cortex, this means that the maps should accurately reflect the underlying neural representation of the visual field within each cortical visual area. Figure 7 reveals that both random-mapped and phase-mapped data for V1 show 2 or even 3 fold differences in the number of voxels responding preferentially to visual field locations near the horizontal meridians compared to the vertical meridians. In an ongoing study from our lab, we have argued that this irregularity likely reflects the effects of midline vasculature structures that alter BOLD signals by introducing excessive noise or atypical temporal phase delays. Such distortions may be inevitable as long as the signals arise from vascular-based mechanisms.

The uneven representation of the visual field can obscure the detection of a true scotoma especially for random multifocal mapping which divides the visual field into a coarse array of stimulus segments. For instance, if a segment stimulates a region encompassing a scotoma plus a portion of responsive cortex, then the net number of voxels responding to this segment might appear similar to the number of voxels responding to some other segment that normally activates fewer voxels. On the other hand, phase mapping provides a continuous encoding of the visual field locations. The higher spatial resolution could facilitate the detection of a scotoma.

Identification of spatially complex pRFs

A region in the visual field that stimulates a voxel in the visual cortex is termed population receptive field (pRF) of that voxel (Dumoulin and Wandell, 2008). Pathologies such as albinism and achiasma can cause abnormal routing of optic fibers, which can induce changes in visual cortex maps. For instance, voxels can have two mirror imaged pRFs in the two hemifields, where the employment of phase mapping requires mapping of one hemi-field at a time (Hoffmann et al., 2003; Sinha and Meng, 2012). If such complex receptive fields are not detected independently, temporal phase mapping will typically assign the pRF to a single erroneous location. In general, if a voxel contains multiple populations of neurons with different pRF locations, the retinotopic assignment with phase mapping may be incorrect or at least incomplete, due to the fact that the sum of multiple sinusoidal waveforms with the same period but different phases is, if not zero, a sinusoidal waveform with a phase different from any of the original phases. Random multifocal stimulation can potentially identify the different components of a complex pRF. Indeed, in a previous study using voxel sizes of 3.75x3.75x4.0 mm, we were able to identify voxels responsive to multiple separate visual field locations (Ward et al., 2012). Voxels having spatially complex receptive fields are also a concern for pRF modeling studies which typically assume that a single Gaussian sensitivity profile is adequate (Amano et al., 2009; Dumoulin and Wandell, 2008; Harvey and Dumoulin, 2011). Though reasonable for most voxels in healthy individuals, this may not be adequate for studies involving visual system pathology or abnormal reorganization. In such cases, random multifocal mapping might be used initially to identify pRFs with multiple components, followed by drifting bars or other stimuli to map the pRF at high resolution.

Stability of Eye Fixation

For the subject tested, the weighted standard deviations and BCEA dimensions are all less than one degree and do not have a significant offset relative to the true center of the stimulus display. Moreover, there is no obvious major difference between the multifocal and phase mapped stimuli (compare BCEA ellipses). Consistent with these results, Baseler et al., 2002 reported that simulation of random eye movements drawn from a Gaussian distribution (mean deviation zero, std. dev. 1 degree) only increased the variance in the results of phase mapping (Baseler et al., 2002). In the same study, they also reported a case of congenital nystagmus of 3 degrees peak-to-peak amplitude. The visual field eccentricity map differed from normal only in the degree of noise in the data. The author suggested that fixation instability simply tends to locally smear the retinotopic maps thus reducing activity.

In the future, routine eye tracking within the scanner may become clinically feasible and necessary, though currently no critical clinical treatment decisions that we know of depend on this degree of mapping accuracy.

Conclusion

The use of fMRI for clinical applications such as pre-surgical mapping impose constraints such as time efficiency and mapping completeness which may be of higher priority than for academic research. MRI scan time is a major factor affecting scan success as well as the number of patients that can be scanned per day. Completeness is important in order to ensure that a functionally critical structure near a site of pathology is mapped as fully as possible so that the neurosurgeon can avoid damaging eloquent cortex and causing post-operative deficits. Compared to random multifocal

mapping, temporal phase mapping was fundamentally more efficient and able to map extrastriate visual areas more completely. Its shortcomings such as retinotopic misassignments caused by noise and hemodynamic variations are modest and likely not to be critical for most clinical applications unless retinotopy with very high precision is needed, as might be the case when trying to assess rehabilitation-induced recovery of cortical function near the margin of a scotoma. Random multifocal mapping provides simultaneous eccentricity and angle mapping, and does not need hemodynamic calibration. But spatial resolution is limited by the number of stimulus segments and its inability to fully map extrastriate visual cortex may limit its utility when a pathology involves lateral or dorsal occipital cortex. With increased noise, random multifocal mapping will virtually always provide a correct retinotopic assignment but the number of significant voxels may be reduced. In short, though phase mapping is probably the better choice for clinical applications such as pre-surgical brain mapping, random multifocal mapping also offers some unique advantages that might be optimal for some specific applications.

CHAPTER 4 VISUAL FIELD MAPPING COMBINING PHASE-ENCODED AND EVENT-RELATED STIMULI

In this chapter, we aim to develop and test a combined visual field mapping paradigm that takes advantage of both phase-encoded and event-related designs.

Introduction

Phase-encoded experimental design

Phase-encoded stimulation paradigms for fMRI were first developed to map the retinotopic organization of human visual cortex (DeYoe et al., 1996; Engel et al., 1997; Sereno et al., 1995). This stimulation method is termed temporal phase mapping in that locations in the visual field are stimulated sequentially, thereby allowing the voxels responding to each location to be identified by the temporal phase of their responses. Over the years, it has been adopted by many different applications while the retinotopic mapping is still the most commonly used one. Multiple mirror-symmetric novel cochleotopic maps covering most of the core and high-order human auditory cortex within and around the superior temporal sulcus were found with phase-encoded fMRI experiments (Striem-Amit et al., 2011). Somatotopic maps of human body surface (Huang and Sereno, 2007) and fingers of one hand (Sanchez-Panchuelo et al., 2010) were delineated by phase-encoded tactile stimulation. Phase-encoded stimulation was also popular in identifying the topographic map of orientation preference in human primary visual cortex (Freeman et al., 2011; Swisher et al., 2010).

Phase-encoded mapping has been widely used since its invention, due to its ability to measure neural activities in a parameterized set of experimental conditions

(Engel, 2012). For example, stimuli stimulating visual eccentricity are presented continuously in the order specified by the eccentricity. The continuous nature of phase-encoded mapping provides high spatial resolution. The focal presentation of stimulating patterns draws visual attention, which can potentially increase the signal to noise ratio. On the other hand, the dependence on exact timing of the fMRI signals of phase-encoded mapping makes it susceptible to hemodynamic variations, which can vary both across people and across different cortical areas. (see Chapter 3 for detailed description of the advantages and weaknesses of phase-encoded mapping).

The distorted retinotopic locations assigned to each voxel can be manually corrected based on the well-established principles that voxels from one hemisphere primarily respond to the contralateral visual hemi-field, and that going from occipital pole anteriorly the voxels preferred visual field locations shift from fovea to periphery. This correction can also be achieved with fMRI scans using stimuli moving in opposite directions, such as clockwise versus counterclockwise rotating wedges or expanding versus contracting rings (Sereno et al., 1995). For each voxel, the phases obtained with stimulus moving in opposite directions can be averaged to cancel out the phase shift caused by the delay of hemodynamics. Then the time series, corrected for this phase shift, acquired with stimulus moving in opposite directions can be averaged for improved SNR.

Event-related experimental design

In event-related designs, events (stimuli/task) are presented in randomized order and the time in between events can vary. The fMRI response is modeled as the linear summation of the hemodynamic response to discrete events. One advantage of event-related designs is the ability to detect variations in the hemodynamic response (the HRF

(Buxton et al., 2004)), thereby allowing characterization of BOLD temporal properties. Different brain regions can have different HRFs although all are active to the same event (Saad et al., 2001). Finally, the variable interstimulus interval (ISI) can also reduce the subject's ability to predict when and what event will happen, thus maintaining the attention level (Amaro and Barker, 2006; D'Esposito et al., 1999).

An improvement on the original event-related design was made after the demonstration of linearity of fMRI signals (Boynton et al., 1996), which allowed the hemodynamic responses from different stimuli to overlap. This improved design is termed rapid event-related fMRI, where the ISIs are shorter than the duration of the HRF. One rule of thumb for the rapid event-related design is that ISIs should be varied, so that deconvolving the overlapping HRFs is possible according to reasonable assumptions of linearity (Amaro and Barker, 2006). The success of rapid event-related designs permitted the progression to more complex experimental paradigms, which played a key role in the widespread application of fMRI to studies of human cognition (Liu, 2012).

An event-related design was applied to retinotopic mapping in a multifocal paradigm, where multiple flickering, checkered segments turning ON and OFF randomly were used as the visual stimuli (Hansen et al., 2004; Vanni et al., 2005). Through a multiple linear regression analysis with the random stimulating sequences as regressors, responses to one or more stimulus segments can be determined for each voxel. Identifying the stimulating segments by their random temporal patterns rather than their response timing (temporal phases) provides a direct link between voxels and visual field locations that is not distorted by the hemodynamic variations. However, the low spatial resolution and ineffectiveness in extrastriate visual areas of such multifocal paradigm compared to phase-encoded paradigm limit its usefulness in both research and clinical

applications.

Mixed experimental design

An event-related design can be mixed with the classic block design to simultaneously model the transient, specific stimuli related BOLD signal, and the sustained, state or mode related BOLD signals. Such mixed design is capable of identification of multiple temporal codings that suggest possibility of ROIs performing separate/multiple processes that act over different timescales (Petersen and Dubis, 2012). Given the different strengths and weaknesses of phase-encoded and event-related designs for retinotopic mapping, a mixed stimulation paradigm taking advantage of both designs could be beneficial as long as the signals evoked by the two designs can be separated.

In this study, we combined phase-encoded and event-related stimuli in a manner that allowed them to appear perceptually independent. A finite impulse response model analysis and a correlation coefficient analysis were used to extract signals to the two types of stimuli. This combined stimuli achieved automated calibration of voxels' temporal phases distorted by hemodynamic delay, estimation of the shape of the hemodynamic response function and simultaneous mapping of phase-encoded retinotopy and selected ROIs of the visual field.

Methods

Subjects

Five subjects (four female), 18-30 years old, participated in this study. All subjects

had normal or corrected-to-normal visual acuity and provided informed, written consent in accordance with methods approved by the Institutional Review Boards of both the Medical College of Wisconsin and Marquette University. Two subjects were scanned with a 3T long bore scanner, and the rest were scanned with a 3T short bore scanner. See Table 2 for detailed experimental arrangements.

	Subject 1	Subject 2	Subject 3	Subject 4	Subject 5
Combined Eccentricity	None	2 repetitions	6 repetitions	6 repetitions	2 repetitions
Combined Polar Angle	3 repetitions	2 repetitions	6 repetitions	6 repetitions	2 repetitions
Conventional Eccentricity	None	2 repetitions	None	None	2 repetitions
Conventional Polar Angle	3 repetitions	2 repetitions	None	None	2 repetitions
Scanner	Long Bore	Long Bore	Short Bore	Short Bore	Long Bore
Minimum ON period Length	10 sec.	10 sec.	10 sec.	10 sec.	2 sec.

Table 2. Experimental arrangements for each subject. The 6 repetitions of combined eccentricity and polar angle mapping for subject 3 and 4 were acquired on two different days. 3 repetitions per day comprised one dataset. The minimum ON period length refers to the length of the shortest ON block in event-related time sequences.

Visual stimulation

At the long bore scanner, visual stimulation was presented via a custom back-projection system. Stimulating images were displayed via a Sharp XG-C330X color video projector, which provided a black/white contrast of 96% superimposed on a

uniform gray background of 265 cd/m^2 . Luminance levels for black and white were 23 and 1120 cd/m^2 respectively.

At the short bore scanner, visual stimulation was presented via a custom back-projection screen. Stimulus images were displayed via a BrainLogics BLMRDP-A05 MR digital projector, which provided a black/white contrast of 99% superimposed on a uniform gray background of 173 cd/m^2 . Luminance levels for black and white checks were 2.04 and 823 cd/m^2 respectively.

At both scanners, the stimulating images were generated using a ViSaGe visual stimulus generator by Cambridge Research System*. Subjects were provided with a 20° radius field of view and asked to passively fixate, throughout the stimulus presentation, on a green marker within 0.1° radius of the center of the display. All stimuli consisted of 8 Hz flickering checkerboard patterns.

The combined stimulus consisted of a conventional phase-encoded component comprised of black/white checks, and event-related components comprised of yellow/gray checks. Figure 14 shows single 2 sec. stimulus frames and stimulus timing waveforms of the two components and their sum at the location labeled by the red dot.

To map the eccentricities of 0.66° to 20° with the phase-encoded ring, this range was divided into 16 elementary rings scaled according to the retino-cortical mapping function reported by Schira et al. (Schira et al., 2010; Schira et al., 2007) so as to achieve theoretically equal areas of activation. At the beginning of each run, the phase-encoded ring consisted of just the center segment (area within 0.66°), and then it recruited one more elementary ring each 2 sec. until the center segment plus 3 elementary rings were included. Then the phase-encoded ring shifted outward by one elementary ring every 2 sec. until it slowly disappeared in steps at the outer margin of the display. The display was uniform gray for 2 sec. Then the sequence repeated from

the center. As shown in Figure 14A, the event-related ring spanning eccentricity 3.30° - 6.77° was turned ON or OFF according to a pseudo-random sequence. To map polar angles, a phase-encoded wedge, spanning a quarter of the visual field, rotated counter-clockwise in 20 steps. At the beginning, the center of the wedge was at the lower vertical meridian. Two event-related wedges spanning 18° each centered at either horizontal meridian were turned ON and OFF using two different pseudo-random sequences (Figure 14B).

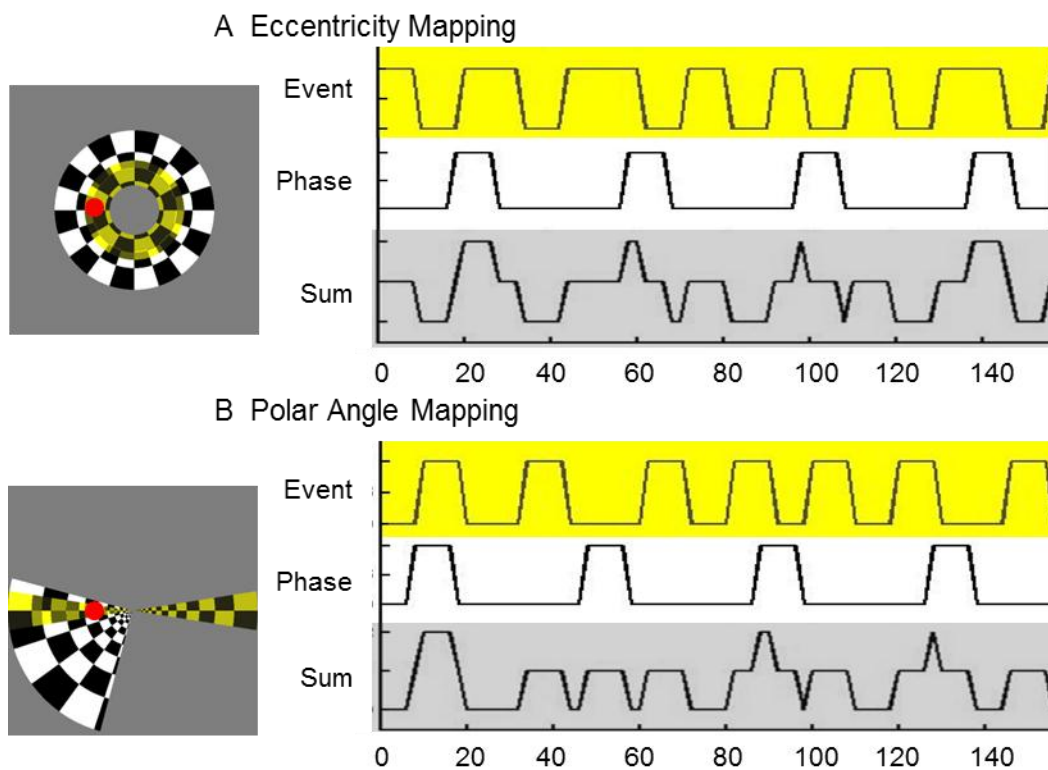


Figure 14. Combined stimuli. Sample stimulating sequences are shown for the visual field location labeled by the red dot.

To achieve sufficient modulation, the ON periods in the pseudo-random sequences were set to be at least 10 sec. long with four subjects. With the other subject we used true random sequences, which could have ON and OFF periods of any length. The event-related ring/wedge appeared to be semi-transparent so that both phase-encoded and event-related components could be seen when they overlapped.

To evaluate the combined method, we also acquired data with conventional phase-encoded mapping with three of our subjects. The conventional phase-encoded stimuli were set to be identical with the phase-encoded components of the combined paradigm. For both combined and conventional phase-encoded mapping, the expansion of the phase-encoded ring and rotation of the phase-encoded wedge were repeated 5 times per run for a total of 200 sec. See Table 2 for detailed experimental arrangement for each subject.

Post-processing scheme

The fMRI signals evoked by the combined stimuli comprised one phase-encoded component and one event-related component. Two analyses, a finite impulse response (FIR) model (Dale, 1999) sensitive to the event-related component and a cross-correlation analysis sensitive to the phase-encoded component, were used in parallel, as illustrated in Figure 15. See subsequent sections for detailed explanations for each analysis.

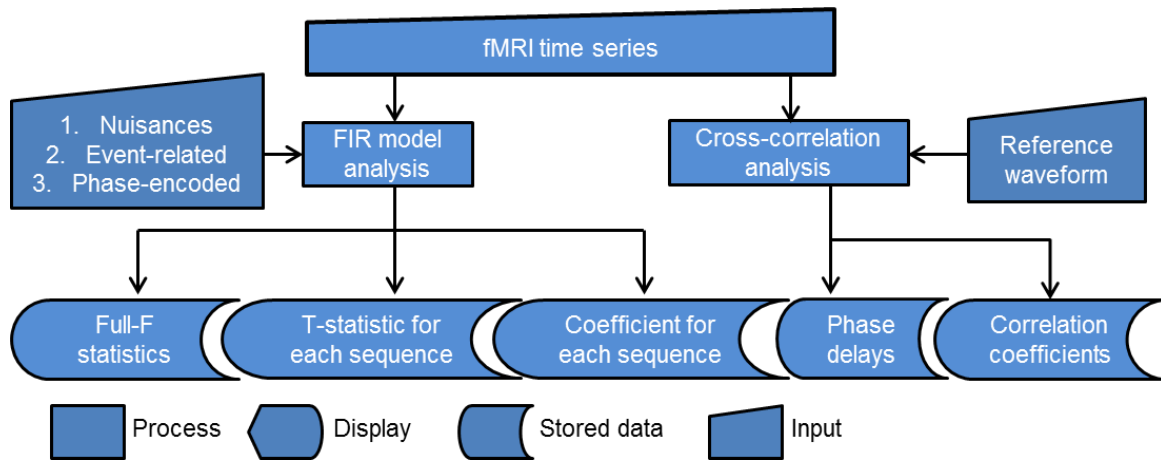


Figure 15. Processing scheme for combined design.

Finite impulse response model

In the FIR model, the BOLD signal was assumed to be a linear, time-invariant system with respect to the stimulus. An HRF was estimated for each event-related stimulus using the set of shifted event-related time sequences as regressors. No assumption on the shape of the HRFs was made. As an example, Figure 16 shows the FIR model for combined polar angle mapping in the matrix format (The FIR models were different depending on the number of event-related stimuli). Legendre polynomials of first to fourth orders were used to model the base line and low frequency fluctuations (Kay et al., 2008), as shown in Figure 16A. The two random binary sequences of the event-related stimuli were cyclically shifted up to 10 steps (20 sec.), and all shifted versions of these sequences were used as regressors, shown in Figure 16B. The coefficients of each shifted sequence formed an estimation of the HRF associated with each event-

related stimulus. In addition to the event-related stimuli, the two horizontal meridians were also stimulated by the phase-encoded stimuli, which also need to be included in the model. Therefore, additional regressors, periodic boxcar sequences convolved with a canonical HRF from AFNI (The canonical HRF was a gamma variate function $HRF(t) = t^{8.6} * e^{-t/0.547}$, where t represents time in seconds (Cohen, 1997)), were used to model the phase-encoded signal in voxels responding to the horizontal meridians, shown in Figure 16C.

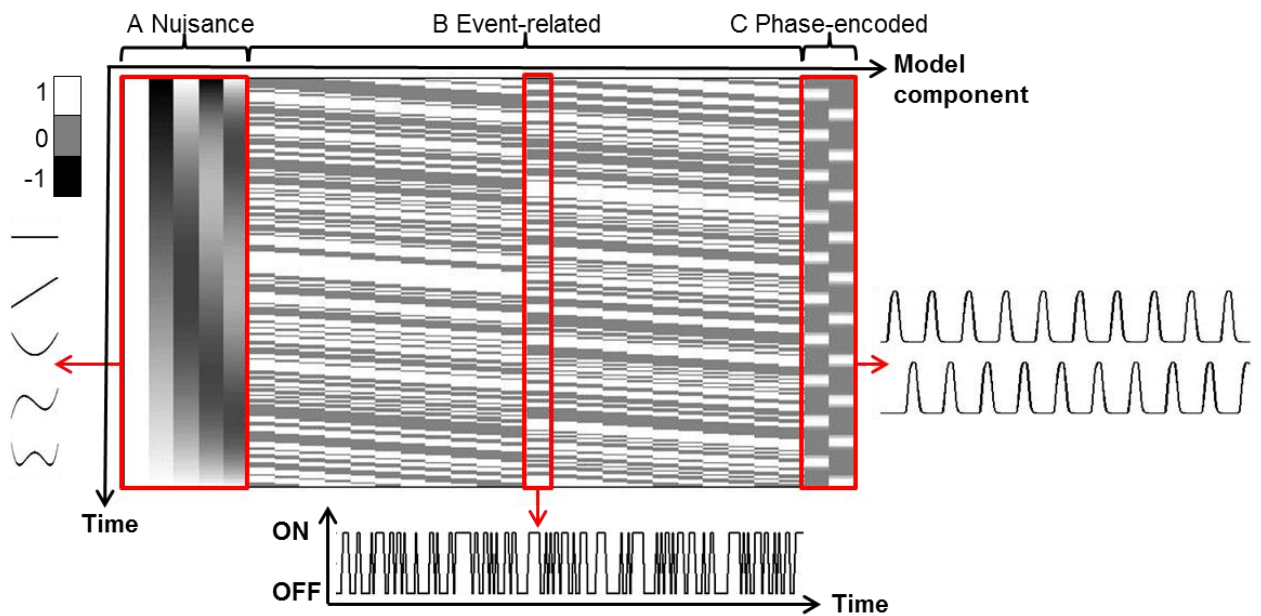


Figure 16. Data model sensitive to event-related signals. Red arrows point to the 1D plots of the model components in corresponding red squares. A. Baseline and low-frequency fluctuations modeled by Legendre polynomials. B. Shifted random sequences for event-related yellow/gray wedges at right and left horizontal meridians. C. Phase-encoded sequences convolved with an estimation of the HRF at right and left horizontal meridians.

The individual components of this FIR model were scaled with different coefficients to fit the fMRI data, as expressed in $y = Eh + Pc + Sb + n$. In this equation, y is the fMRI data; E is the matrix of shifted event-related sequences (Figure 16B), h is the vector comprised of the HRFs to the event-related stimuli; P is the matrix of phase-encoded periodic sequences (Figure 16C); c is the matrix of coefficients associated with each phase-encoded sequence; S is the nuisance matrix (Figure 16A); b is the set of nuisance coefficients; n is the noise. This FIR model analysis estimated h , c , b , n , as well as a full-F statistic for the overall goodness of fit and a t-statistic for the goodness of fit of each coefficient.

Cross correlation analysis

As described above, the FIR model was restricted to be only sensitive to voxels that responded to the event-related signals, in that the model components only included the event-related time sequences and phase-encoded sequences with phases roughly corresponding to the locations of the event-related stimuli. A cross-correlation analysis was also performed as in the conventional temporal phase mapping experiments to make use of the phase-encoded signals (Bandettini et al., 1993; Saad et al., 2003). The reference waveform used for cross-correlation analysis was simulated neural signal, which is essentially the fMRI signal without the smoothing effect of the HRF, at the onset locations of the phase-encoded stimuli, based on a modified version of the pRF model proposed by Dumoulin and Wandell (Dumoulin and Wandell, 2008). Specifically, a 2D Gaussian sensitivity profile, the pRF, centered at the onset locations of the phase-encoded stimuli was convolved with a series of binary images of the phase-encoded stimuli. The standard deviation of the pRF was adjusted according to previously published data for the scaling of pRF size across eccentricities (Harvey and Dumoulin,

2011). The resulting waveform simulated the neural signal at the onset location of phase-encoded stimuli, and was used as the reference waveform for cross-correlation analysis. Using such a reference waveform, the resultant phase shift of each voxel reflected the distance from the voxel's pRF to the onset location of the phase-encoded stimuli plus phase shift induced by the hemodynamics.

Evaluation of the combined design

A potential concern about adding the event-related components to phase-encoded stimuli is possible disruption of the phase-encoded retinotopic mapping. The altered contrast level at visual field regions with event-related components might alter the signal strength. Therefore, we compared the signal power and correlation coefficients with the reference waveform between voxels responding to visual field regions with and without the event-related stimuli.

To identify voxels responding to visual field locations with and without the event-related stimuli, a histogram of temporal phases of voxels with significant ($p < 0.05$) full-F statistics was plotted, as shown in Figure 17A. The peaks of this histogram indicated phases/visual field locations with the event-related stimuli, in that the majority of voxels with significant full-F statistics were responsive to the event-related stimuli. Therefore, one two-second bin was selected at the peak as the visual field region with event-related stimuli, termed combined region. One other two-second bin was selected off peak as the visual field region with phase-encoded stimuli only (No bin was selected at the trough to avoid naturally under-represented vertical meridians (Janik et al., 2013)). The combined and phase-encoded regions are labeled by yellow and black shades in Figure 17A. The powers and correlation coefficients of voxels within each of the two-second bins were averaged. The averaged power and correlation coefficient of each region were then

averaged across five data sets- combined polar angle mapping of subject 1, combined eccentricity and polar angle mapping for subject 2 and 5. Bin selection was random as long as it was within the required range to minimize potential regional effect.

We also compared the assigned temporal phases by the combined stimuli and conventional phase-encoded stimuli to address the potential issue of altered retinotopic assignments by adding the event-related stimuli. These analyses were performed using AFNI package (Cox, 1996b). With subjects 1, 2 and 5, we performed multiple repetitions of both combined and phase-encoded mapping (See Table 1 for detailed experimental arrangements). For each mapping paradigm with each subject, we randomly picked one repetition of combined mapping and two repetitions of phase-encoded mapping. A scatter plot was created of the temporal phases from the one repetition of combined mapping versus the one repetition of phase-encoded mapping. A second scatter plot was created of the temporal phases between the two repetitions of phase-encoded mapping. Only voxels with correlation coefficients greater than 0.4 from both repetitions were included in the scatter plot between the two.

Calibration of the phase-encoded retinotopic locations

With a few extra processing steps, the combined paradigm can achieve an automated calibration of the temporal phases assigned by the phase-encoded stimuli.

In contrast to the ambiguous link between visual field locations and temporal phases of voxels, responsive voxels to the event-related stimuli had known responding locations, and thus can be used to calibrate the voxels temporal phases. As stated previously, FIR model analysis output a coefficient and a T-statistic for each model component, and a full-F statistic for the whole model. We selected a pre-determined number of voxels with the highest full-F statistics. A histogram was made of the phase

shifts of these selected voxels along one sec. bins from 0 to 40 sec. This histogram was then correlated with a reference histogram at different shifted phases. The phase with the highest correlation coefficient was taken as our estimation of phase shift caused by the hemodynamics, which was subtracted from the phases of all voxels to generate corrected retinotopy. The reference histogram was generated using the same modified pRF modeling described above. Specifically, we simulated 800 fMRI responses to the combined stimuli without HRF smoothing. The reference histogram was constructed using the 100 simulated responses with the highest full-F statistics.

The accuracy of this calibration was evaluated through comparison with the manual calibration through FFMMap described in Chapter 2.

Results

Evaluation of the combined design

Overall the combined design showed no significant difference in retinotopic mapping from the conventional phase-encoded design except for the increased signal power, which is not a critical factor in retinotopic mapping. Furthermore, the power difference is, although significant, still modest ($p=0.045$). The difference in power is only 24% of the power of the combined region.

The averaged power and correlation coefficient in combined and phase-encoded regions are shown in Figure 17B and 17C. No significant difference in correlation coefficient existed between combined and phase-encoded regions. However, a significant difference was observed in power between the two regions. The altered power of the signal is unlikely to have any impact on retinotopic mapping, which only depends on the temporal phase and correlation coefficient with the reference waveform.

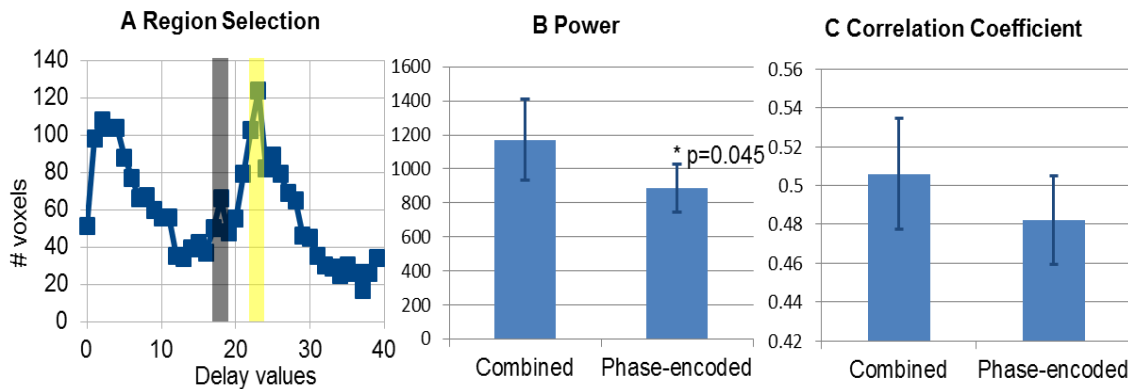


Figure 17. Power and correlation coefficient of voxels responding to visual field regions with and without event-related stimuli. A. A sample histogram of temporal phases of voxels with significant full-F statistics from combined polar angle mapping for one subject. Regions with and without event-related stimuli are labeled with yellow and black shades. B. Power and C. Correlation coefficient of voxels responding to the combined region and phase-encoded region, averaged across all subjects.

The temporal phases of the same voxels assigned by combined mapping and phase-encoded mapping were compared in scatter plots to address the issue of potential disruption of the event-related stimuli to phase-encoded retinotopic mapping. Figure 18A and 18C show the visually most disparate plots across all the three subjects for whom both combined and phase-encoded data were acquired. Figure 18B and D show the plots between two repetitions of phase-encoded mapping of the same subject

as references (Data in panel A and B are from the same subject, Data in panel C and D are from the same subject). Total numbers of voxels included in Figure 18A, B, C and D are 4021, 4910, 4780 and 5501. (The shown temporal phases were corrected for wrap-around). The fitted linear trend line is shown as the black straight line. The corresponding equation of the linear trend line is also displayed in each plot. Qualitatively the scattering between temporal phases from combined and phase-encoded mapping is on the same order with that between phases from two repetitions of the same phase-encoded mapping. A subsequent t-test on the slopes of the trend lines across all subjects showed no significant difference ($p > 0.05$) between the two types of scatter plots.

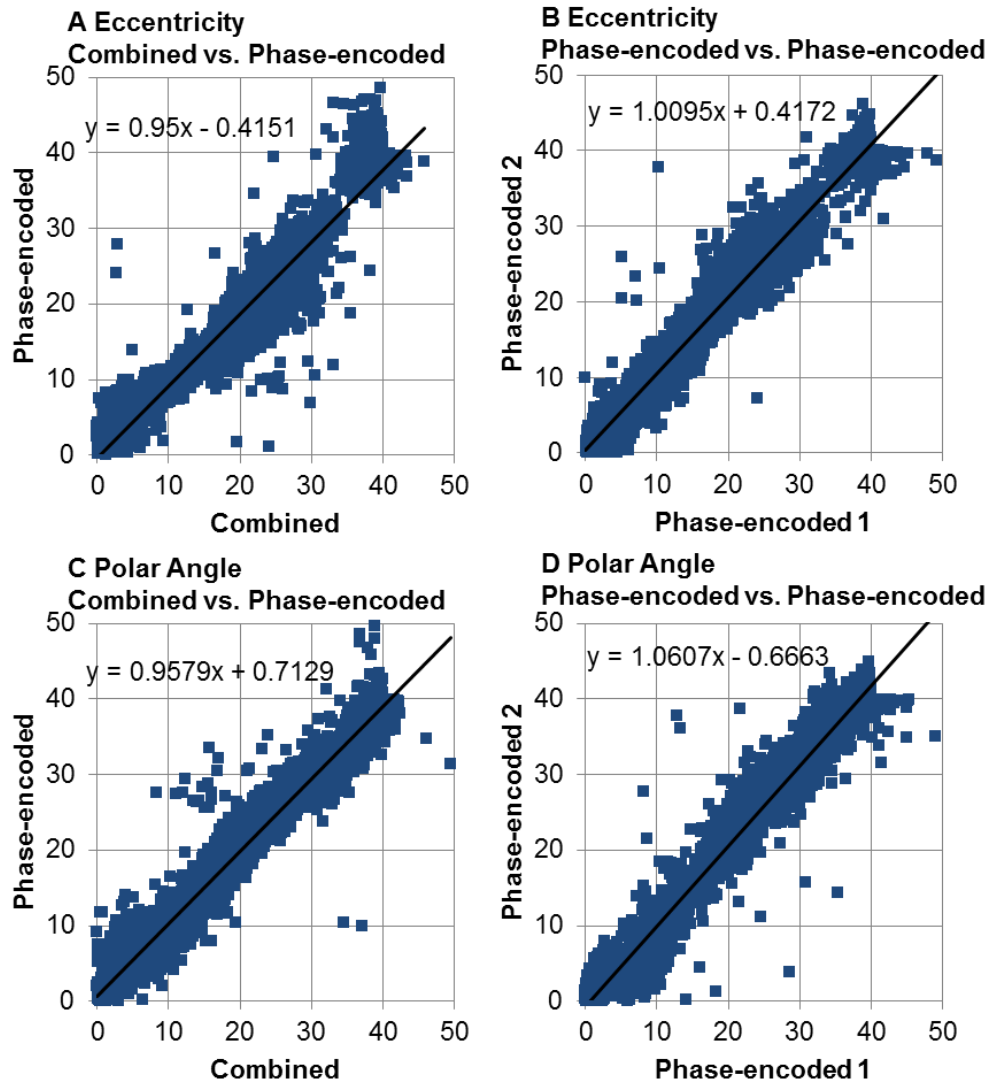


Figure 18. Comparison of temporal phases between combined design and phase-encoded design. Visually most scattered plots between combined and phase-encoded designs are shown in A for eccentricity mapping, and in B for polar angle mapping. Scatter plots between two repetitions of phase-encoded mapping are shown in B and D. Black straight line shows the linear trend in each scatter plot.

Applications of the combined mapping

Three applications of the combined design, calibration of voxels temporal phases, simultaneous mapping of the retinotopy and selected ROIs, and estimation of

the HRF for each event-related stimulus, were demonstrated.

- *Calibration of voxels temporal phases*

The voxels that responded to the event-related stimuli were used to calibrate the temporal phases of all active voxels taking advantage of their known responding locations.

The entire post-processing sequence, including the calibration process, was fully automated and took about 15 minutes for an fMRI data set containing approximately 420,000 voxels. This automated calibration generated comparable results with the manual calibration method described in Chapter 2. Table 3 lists the temporal phases caused by the hemodynamics estimated using combined mapping and the manual calibration, as well as the minimum, maximum and averaged absolute differences between the two methods. The difference between combined mapping and manual calibration is generally smaller for polar angle mapping than for eccentricity mapping ($p < 0.05$). Given that the variations of fMRI signal in time caused by noise is about 2 seconds (Saad et al., 2001), any difference smaller than 2 seconds is probably not significant.

	Eccentricity		Polar Angle	
	Comb. (sec.)	Manual (sec.)	Comb. (sec.)	Manual (sec.)
Subject 1	NA	NA	5	4.7
Subject 2	6.5	4	4.5	4.1
Subject 3 (Day 1)	5.5	2.8	4	4.7
Subject 4 (Day 1)	7	3	3	3.4
Subject 3 (Day 2)	7	3.5	3.5	3.7
Subject 4 (Day 2)	6	3.7	4	4.7
Subject 5	5	4.1	4	4.2
Min. Diff.	0.9		0.2	
Max. Diff.	4		0.7	
Ave. Diff.	2.65		0.41	

Table 3. Difference in estimations of the temporal phases caused by hemodynamics from the combined mapping and manual calibration.

- *Simultaneous mapping of retinotopy and selected ROIs*

Voxels responding to the event-related stimuli were identified based on their significant full-F statistics from FIR model analysis. By coloring voxels with their respective full-F statistics, maps of the visual field regions stimulated by the event-related stimuli were obtained in addition to the phase-mapped retinotopic maps.

Figure 19 shows four sets of flattened brain surface maps for subject 2. (fMRI

time courses were spatially filtered by a 3.5mm averaging kernel for display in Figure 19. FMRI data used in all other analyses were not filtered spatially or temporally.) In panel A and B, the flat maps are colored by temporal phases from combined eccentricity and polar angle mapping. In panel C and D, the flat maps are colored by full-F statistics from the FIR model analysis. It is obvious that voxels with high full-F statistics formed bands along the representation of middle eccentricities, label by white dotted lines in the color pinwheel in panel A, and horizontal meridians. The regions with high full-F statistics in panel C were also delineated by white dotted lines in panel A to show the correspondence between the representations of the event-related ring and visual field eccentricities. For this particular subject, representations of event-related ring were apparent in V1, V2, V3 and V3AB; Representations of event-related wedges, the horizontal meridians, were apparent in V1 and V3AB in both hemispheres, at the boundary between V2 and V3 in the right hemisphere and the ventral half in the left hemisphere. The representation of the right horizontal meridian between left dorsal V2 and V3 is absent in panel D, and only faintly visible in B.

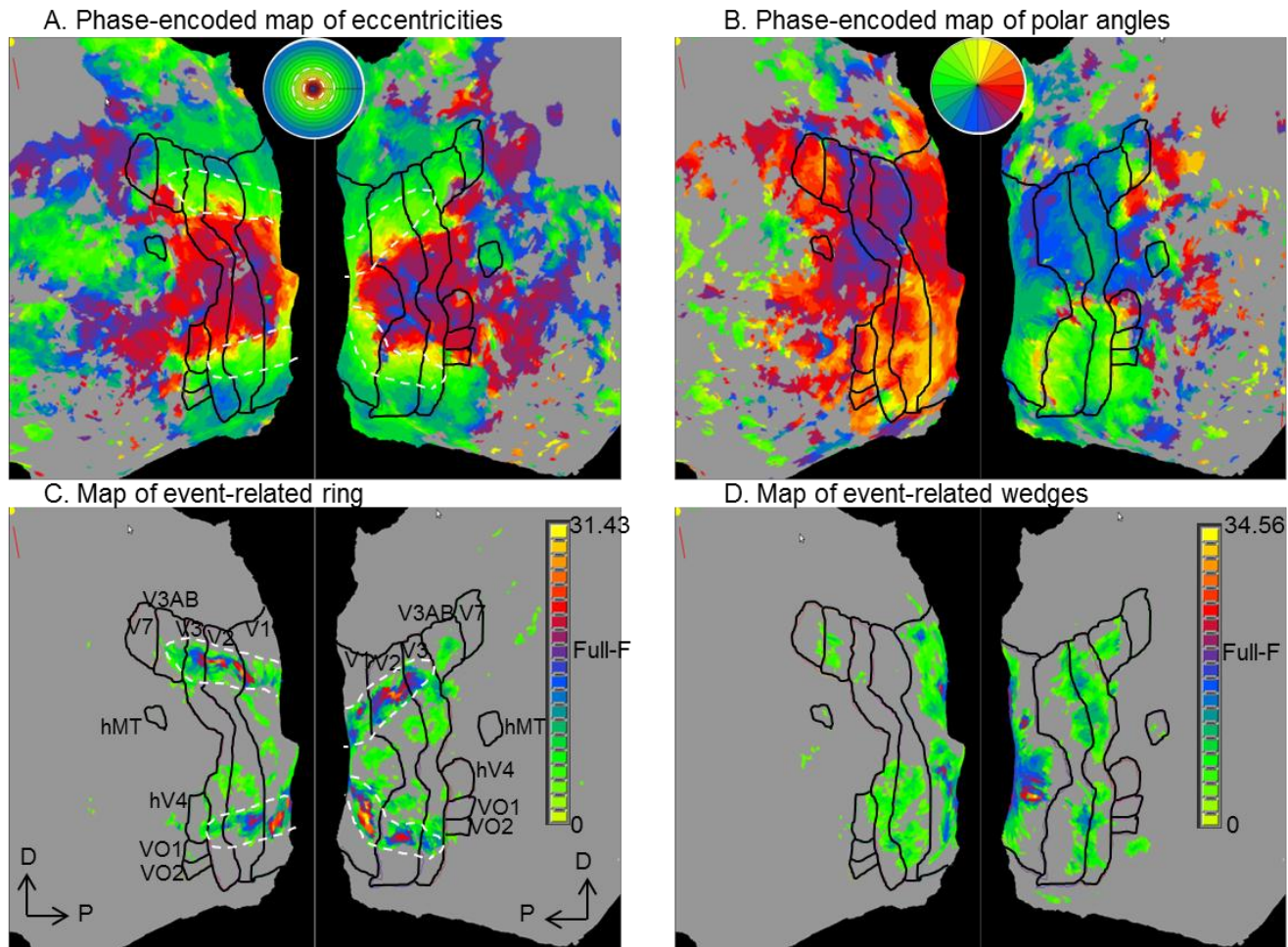


Figure 19. Phase-encoded retinotopy and maps of the event-related stimuli overlaid on flattened brain surface models for one subject. Black outlines denote different visual areas. The color pinwheels in A and B indicate the color code for phase-encoded eccentricities and polar angles. Color bars in C and D indicate the color code for full-F statistics from FIR model analysis. The white dashed lines in D denote the calcarine sulci, where the flat surface can be “zipped” back to form a 3D brain model. Regions with high full-F statistics in C are delineated with white dotted lines, which are copies onto the flat maps in A. The location of the event-related ring is labeled by white dotted lines on the color pinwheel in A as well.

- *HRF estimation*

The FIR model analysis output a coefficient for each shifted version of each event-related temporal sequence. These coefficients were the hemodynamic responses

to the corresponding event-related stimulus at each time point, which together formed an estimation of the HRF to that event-related stimulus. Figure 20B shows such estimations for nine neighboring voxels at the location indicated by the big blue cross hair in Figure 20A, where a high-resolution image of an axial slice of the brain is shown. Data shown in Figure 20 was from the combined eccentricity mapping with subject 5. Such an estimation can be made for every voxel responsive to the event-related stimuli for every subject.

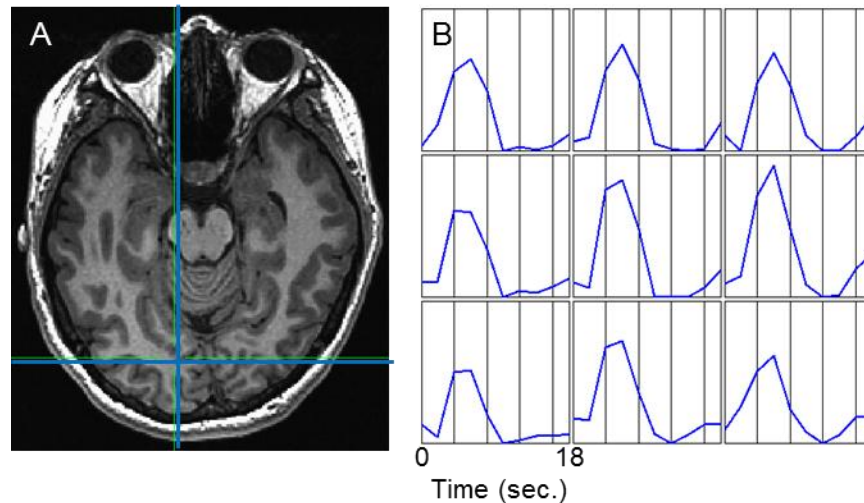


Figure 20. Sample estimations of the HRFs of nine neighboring voxels that are responsive to the event-related stimuli from one subject.

Discussion

We developed a combined visual field mapping paradigm that takes advantage of both phase-encoded design and event-related design by adding isolated event-related stimuli to the conventional phase-encoded stimuli. The results showed that combining the two stimuli had little to no significant impact on the resultant retinotopic maps. In

addition, the combined paradigm provided 3 potential applications, including automated calibration of temporal phases, simultaneous mapping of retinotopy and selected ROIs and estimation of the HRFs for individual selected voxels.

Automated calibration of voxels temporal phases

The timing of the phase-encoded activation at a particular brain voxel is determined by the distance of a voxel's "population receptive field" (pRF) (Dumoulin and Wandell, 2008) from the stimulus onset location plus a delay due to the sluggish hemodynamic mechanism responsible for the fMRI signal. Consequently, the ability to precisely locate the pRF of a given voxel is limited by the accuracy of the estimation of the temporal properties of the signal and the variability of the local hemodynamics. The automated calibration achieved in this study removes a constant hemodynamic delay from all active voxels and thus provides a more accurate estimation of the location of voxels' pRFs. It is more objective and time efficient than the manual calibration process.

Removing the additional phase delay caused by the BOLD hemodynamics can also be achieved with fMRI scans using two stimuli moving in opposite directions, such as clockwise versus counterclockwise rotating wedges or expanding versus contracting rings (Sereno et al., 1995). This method calibrates each voxel individually and thus is more accurate theoretically given that the hemodynamic delay can vary across voxels. The downside of this calibration method is the requirement of an additional fMRI scan.

Estimating HRF for each voxel

An ongoing study from our lab has shown that about 6.3% of the total active voxels that responded to large-field visual stimulation of one subject have inverted HRFs

in their fMRI responses. The inverted hemodynamic response functions were found in all 16 visual areas tested (Puckett et al., 2013). Therefore, an estimate of the shape of hemodynamic response function for each individual voxel might be desired in studies where the profile of hemodynamics is critical.

For the event-related stimuli, we used random sequence with minimum ON block of 10 sec. with subject 1 to 4 to achieve maximum detection power. This specification inevitably reduced the randomness of the sequence, which may introduce more noise in estimating the HRFs. Using an m-sequence (Buracas and Boynton, 2002) or a true random sequence could potentially increase the independence among the time shifted versions of the event-related sequence and thus decrease the noise. Therefore, we used random sequences in which ON and OFF blocks can be any length in the last experiment with subject 5. By visual inspection the HRFs depicted for subject 5 shaped more like the canonical form of the HRF. Additional experiments may be required to demonstrate the tradeoffs between detection power and estimation efficiency of the HRFs in sequence selection for the event-related stimuli.

The estimation of the HRFs for voxels responding to event-related stimuli achieved in this study can be easily generalized to all voxels by expanding the event-related stimuli to whole field. One of the obvious tradeoffs for the whole field design is losing the maps of specific regions of interest, and subsequently the ability to calibrate voxels temporal phases. An alternative design is to add more event-related components to cover the whole field while keeping the sensitivity to specific visual field regions. This design may require longer data acquisition time due to the increased number of parameters to estimate. It may also fail in higher visual areas due to the partial activation of the bigger receptive fields of the voxels in higher visual areas (Ma et al., 2013).

Linearity of fMRI signal and combined mapping

We designed the combined stimuli to achieve perceptual separation of phase-encoded stimuli from event-related stimuli, so that both of them can activate the visual cortex with their distinct temporal sequences. Intuitively the perceptual separation is necessary for the separation of the two signals in each voxel. However, mathematically the separation of the two signals depends solely on the linearity of the response amplitude of the fMRI signals. The BOLD fMRI mechanism has been shown to be a linear time-invariant system (Boynton et al., 1996; Dale and Buckner, 1997), as long as the stimuli have a sufficient temporal duration (Birn et al., 2001), and the amplitude of fMRI response is largely scaled with contrast (Boynton et al., 2012). Therefore, theoretically speaking, the separation of signals is best achieved when the contrast level of overlapping stimuli is manipulated to be twice as much as the contrast of a single stimulus. Presumably the linear scaling of the contrast might also help with the perceptual separation of the two types of stimuli.

In the current combined design, the phase-encoded stimuli (black/white checks) and overlapped stimuli have similar contrasts, which are roughly twice as high as the contrast of the event-related stimuli (yellow/gray checks). It is a suboptimal design mathematically in that the stimuli are not linearly scaled in amplitude as the processing model assumes. Nevertheless, the separation of signals from the current combined mapping was effective, possibly because of the rareness of overlapping of the two stimuli that happened during the scan.

Conclusion

The effectiveness of our “prototype” of combined visual field mapping

demonstrated the feasibility of spatially overlapping stimuli, thus enabling combination of existing visual stimulation paradigms with distinct advantages. The specific design we implemented in this study achieved automated calibration of voxels' temporal phases distorted by hemodynamic delay, estimation of the shape of the hemodynamic response function and simultaneous mapping of phase-encoded retinotopy and selected ROIs of the visual field.

CHAPTER 5 IMPROVE THE SENSITIVITY AND RELIABILITY OF FUNCTIONAL FIELD MAPS FOR DETECTION OF SCOTOMATA

In this chapter, we aim to develop a prototype of probability-based FFMap then determine the number of subjects required for a normative probability based FFMap.

Introduction

As briefly introduced in Chapter 2, a functional field map (FFMap) is a diagram of a subject's visual field with circular symbols placed at locations to which voxels have shown a response. Such a diagram is created to directly view the sensitivity profile of the visual cortex from fMRI response. An example of the current FFMap is shown on the right side of Figure 1 (See Chapter 1). The circular symbols can be colored to represent signal strength or retinotopic location of the corresponding voxel. The latter is more commonly used since it provides a direct visual link between a voxel and its responding location for observers, thus making it easier to interpret the functional significance of the brain activation pattern.

The FFMap allows the physician to readily interpret the fMRI cortical maps in terms of visual function thereby assisting the use of fMRI maps for planning surgical treatment of focal brain pathology. However, current FFMap is only a qualitative representation of the visual function served by different cortical regions, which provides little information about the relative probability of obtaining a brain response from different locations within the field of view. To reliably detect impairments in visual responsiveness, a more probabilistic display is needed. The goal here is to develop a method for using existing data from healthy subjects to create an appropriate probabilistic FFMap and

then obtain an initial estimate of variance to permit a power analysis which will help define the number of normal subjects needed to create a normative probabilistic FFMap.

Missing information about pRF sizes

The probability that a brain response can be evoked from a specific visual field location will depend on the number of voxels whose pRF's cover that location. The range of expected response magnitudes for that location will depend on the range of magnitudes obtained from those same voxels. Therefore, the size of each circle in the FFMap correctly representing the size of the voxel's pRF is a key factor in achieving the probabilistic FFMap. Currently the size of a circle is scaled in proportion to the potential error of temporal phase mapping measured empirically at different eccentricity (Saad et al., 2001), due to the fact that a voxel's pRF had not been readily accessible from routine retinotopic mapping experiments using fMRI until recently.

A new computational strategy has been proposed to find both location and size of a voxel's pRF from data generated with the popular phase-encoded mapping (Dumoulin and Wandell, 2008). While it is well accepted that the phase of a phase-encoded signal reflects the voxel's pRF location, previous research has also shown that the temporal duration of the active epoch relative to the inactive epoch of the phase-encoded signal indicates the size of the voxel's pRF (Smith et al., 2001). Using this knowledge of how the properties of a voxel's pRF are reflected in its fMRI signal, the quantitative framework to model the pRF properties was constructed. In this study, we implemented such a modeling process.

Quantitative FMap

Neighboring pRFs on the FMap need to be integrated to one quantity before any probability can be calculated on it. We experimented with quantitative FMap using data from the randomized multifocal mapping we implemented in Chapter 3. The randomized multifocal mapping stimulates the visual cortex with discrete segments, each of which is turned on or off using a different random sequence. Voxels are classified to each segment by their distinct temporal patterns. The number of voxels responding to each segment is the sum of the number of voxels responding to each location that can be differentiated by phase-encoded mapping within that segment. Therefore, the multifocal mapping essentially integrates over the pRFs within each area spanned by one segment, and assigns one quantity to represent the responsiveness of the visual cortex to each area. We believe constructing an FMap for the multifocal mapping is a useful predictor to the quantitative FMap for phase-encoded mapping.

Methods

pRF Modeling

The method proposed by Dumoulin and Wandell models a voxel's pRF by simulating an fMRI visual field mapping experiment using a computational process and fitting the simulated fMRI signals to the empirical fMRI signals. A flow chart of the modeling process is shown in Figure 21, reprinted from Dumoulin and Wandell, 2008 (Dumoulin and Wandell, 2008).

Given the uniform contrast level and flicker rate of the stimulus pattern, visual stimulation is simulated as a binary 2D matrix of ones and zeros covering the entire

visual field, with ones at locations where the stimulation pattern is present and zeros elsewhere. Such a matrix is generated for each time point of the stimulation sequence. Next, the sensitivity profile of a voxel's pRF is modeled as a 2D Gaussian distribution (determined by center location (x_0, y_0) and standard deviation (σ_x, σ_y)). One or more of four parameters, x_0 , y_0 , σ_x , and σ_y , is iteratively modified during the fitting process. At a given time point, the voxel's pRF response is modeled as the effective overlap, calculated as the spatial convolution, between its pRF model and the stimulus pattern at that time point. This effective pRF response time series is filtered by the default HRF in the AFNI package to get the predicted BOLD time course for the individual voxel. The default HRF was a gamma variate function $HRF(t) = t^{86} * e^{-t/0.547}$ (Cohen, 1997), where t represents time in seconds. Finally, a linear fit procedure of this predicted fMRI signal to the empirical fMRI signal is performed. The goodness of fit is estimated by residual sum of squares (RSS). A Matlab optimization routine 'fminsearch' (Lagarias et al., 1998) is used to iteratively modify one or more of the model parameters to minimize RSS. The search process is terminated at convergence of RSS or after 3000 iterations. The search for each voxel's pRF begins at the location identified by the temporal phase of its fMRI signal. Starting size for the pRF can be manually set.

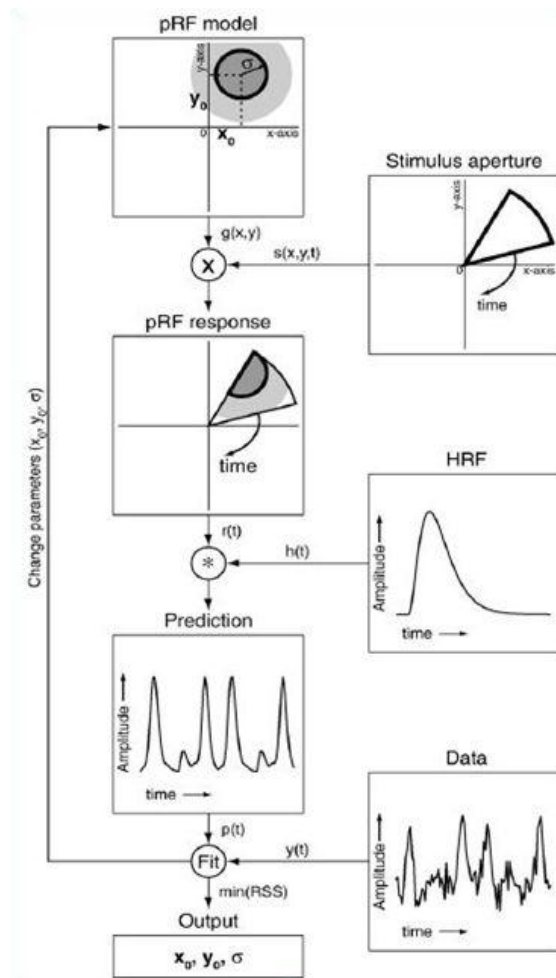


Figure 21. Flow chart of pRF modeling process. Reprinted from Dumoulin and Wandell, 2008 (Dumoulin and Wandell, 2008). The goodness of fit of the simulated fMRI signal to the empirical fMRI signal was assessed using the percent variance in the empirical signal explained by the simulated signal.

Results and discussion

pRF modeling

The pRF model provided fitted simulated fMRI signal for the majority of voxels.

The goodness of fit, represented by the percent variance explained, was found to be

correlated with the correlation coefficient between the empirical signal and a standard sinusoidal waveform, as shown in Figure 22. This result was more or less expected since the correlation coefficient was mainly determined by the SNR of the signal.

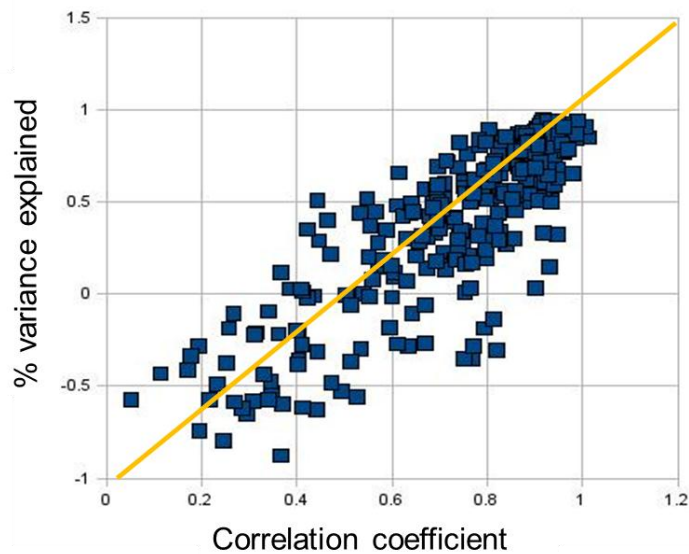


Figure 22. Scatter plot of percent variance explained vs. correlation coefficient for all voxels in V1 for one subject. Yellow straight line shows the linear trend.

For voxels with high SNRs, the phase and time duration of the active epoch of the simulated signal were tightly coupled with that of the empirical fMRI signal, and the resulting size estimations for voxels in different visual areas agreed with the well-established observation that pRFs become progressively larger through the hierarchy of visual areas (Smith et al., 2001), illustrated in Figure 23. However, for voxels with noisier signals, the fitting of the modeled fMRI responses to the empirical fMRI responses may be trapped in a local minimum, which may result in large errors in the pRF estimation.

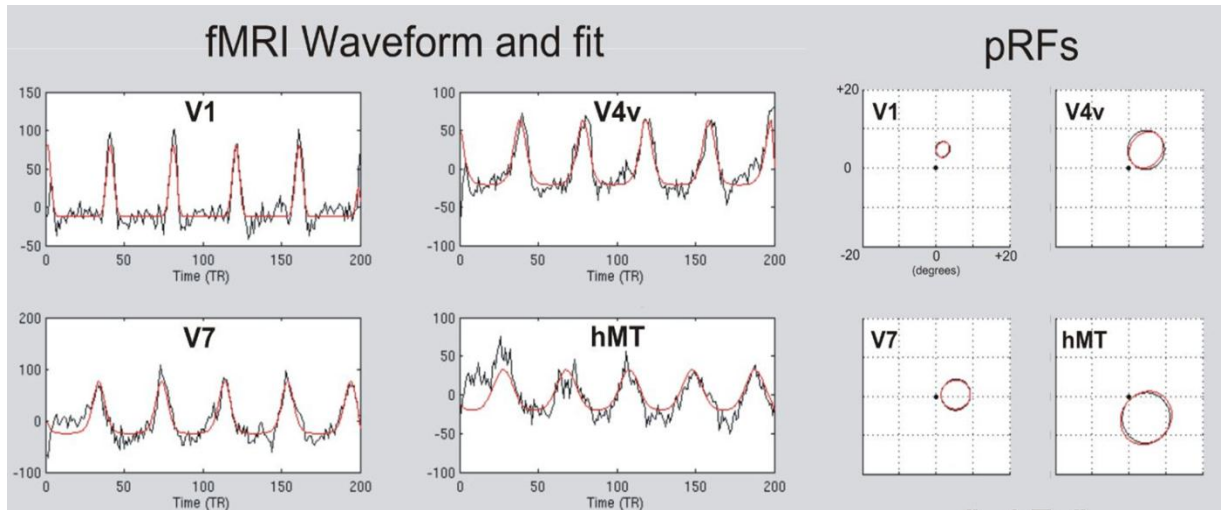


Figure 23. Estimated pRFs for voxels in visual area V1, V4v, V7 and hMT. Simulated signal (red) is overlapped on empirical fMRI signal (black). Outlines of the corresponding pRFs are plotted on the grid to the right, where the center black dot corresponding to the center of gaze of the subject.

Variations in number of pRFs within and across subjects

As explained in the introduction, the randomized multifocal mapping assigns one quantity to represent the responsiveness to the visual field region each segment covers, which, in effect, is the integration of signals over all pRFs within that region. We calculated the number of voxels responding most significantly to each segment as a potential metric for construction of a quantitative FMap.

Figure 24A-E show diagrams of the visual field with each stimulus region colored by the number of voxels responding best to that region. Only voxels within V1 that had significant full-F statistics were included in these diagrams. The number of voxels responding to different regions of the visual field is highly variable for one subject. The

spatial distribution of the voxel count throughout the visual field is also highly variable across subjects. To better appreciate the variation across subjects, each diagram was normalized to the total number of voxels. Mean and standard deviation across the five normalized diagrams were then calculated and shown in Figure 24F-G. Note the color scale in Figure 24G is half of that in 24F, thus the same color in 24G indicates half of the value in 24F. The generally similar color in the same segment in Figures 24F and 24G indicates that the standard deviation is about half the value of the mean.

Invasive animal studies in primates' visual cortex have shown that the underlying neural representation of the visual field is nearly uniform across the entire visual field (Tootell et al., 1982; Van Essen and Zeki, 1978). However, non-uniformities in the coverage of FFMaps has been observed with many subjects using fMRI retinotopic mapping (Janik et al., 2003). Specifically, the proportion of voxels representing the vertical meridians is significantly lower than the proportion representing the horizontal meridians. Some subjects' FFMaps can even miss the representation of the upper vertical meridian completely, therefore showing 'holes' in the upper middle portion of the visual field. These non-uniformities might reflect the distortion of the fMRI signal associated with voxels in the physical location of the representation of the vertical meridian due to the close proximity of the midsagittal sinus and associated draining veins. Non-uniformities across eccentricities might also be caused by various vasculature and noise levels.

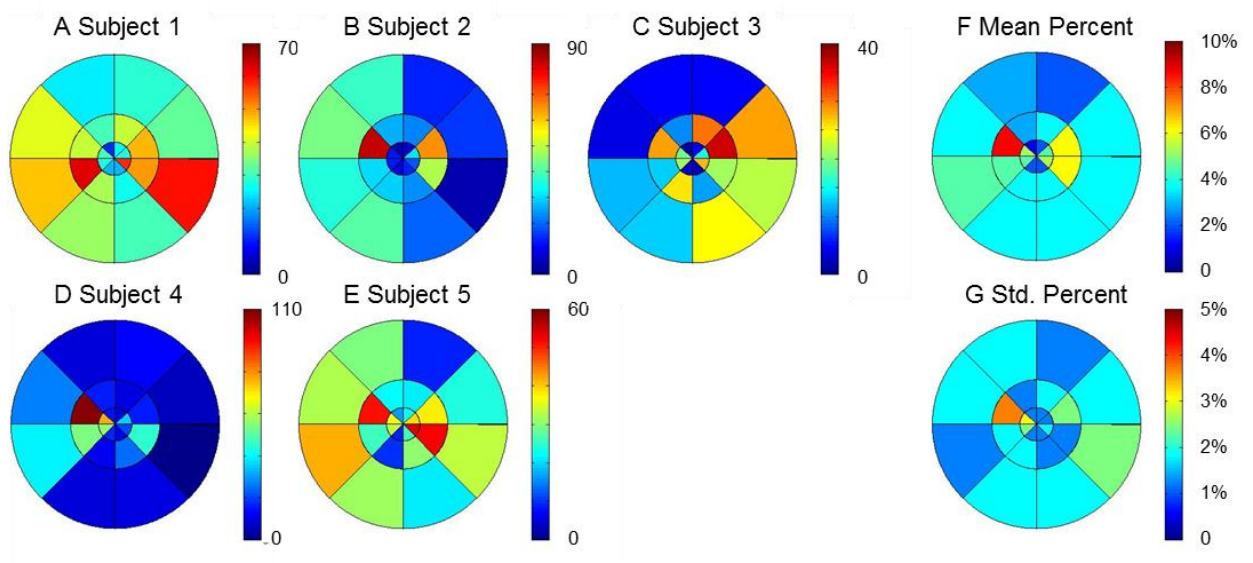


Figure 24. Diagrams of responsive voxel count to each segment. A-E. Diagrams of five subjects. Color in each region represents the number of voxels responding most significantly to that region. F. Mean of the percent voxel count (normalized to the sum of the voxel counts to all segments) across the five subjects. G. Standard deviation of the percent voxel count across the five subjects.

Scotoma detection by quantitative FFMap

One important application of fMRI visual field mapping in clinical practice is the delineation of brain-related scotomata. In the conventional FFMap, scotomata can be easily detected as a hole with few pRFs. To test the ability of scotoma detection of the quantitative FFMap, we placed a circular gray occluder at a fixed location in the upper left quadrant of both random multifocal and phase-encoded stimuli in a separate experiment. With one subject, we tested two such artificial scotomata of 10.9 and 8.5 degrees diameter, as shown in Figure 25A. The renditions of artificial scotomata by random multifocal mapping and phase mapping are shown in Figure 25B-D respectively. For quantitative FFMaps generated with random multifocal mapping, a threshold number was manually selected and applied to the voxel counts to form a binary

representation of the responsiveness of visual cortex to each segment, shown in Figure 25C. For the quantitative FFMMap, the artificial scotomata are only visible in the thresholded binary maps, which implies that the quantitative FFMMap based on voxel count to each random segment is incompetent in revealing scotomata even though the information is present. Note that many other measures can be used to construct quantitative FFMMaps, the capability of which to reveal scotoma is to be investigated.

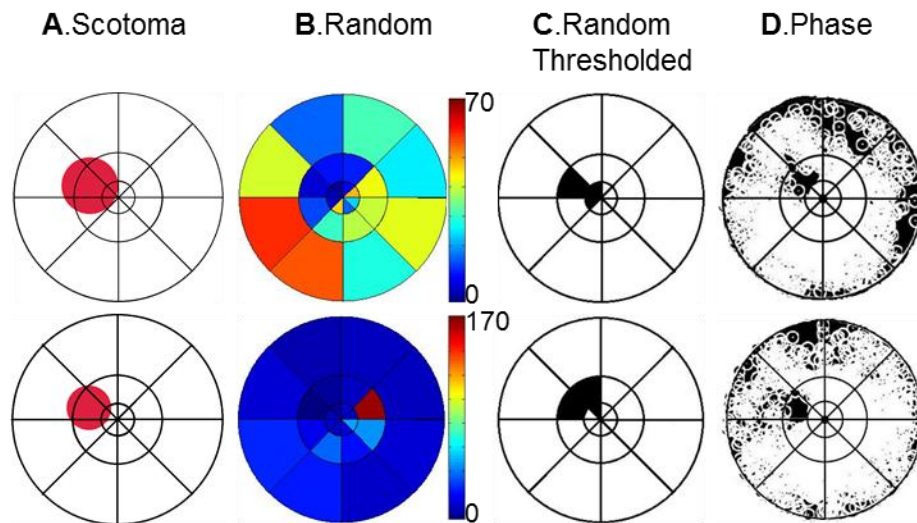


Figure 25. Representation of artificial scotomata by quantitative and conventional FFMMaps. A. Simulated scotomata. B. Quantitative FFMMap: Voxel count evoked by each random segment. C. Thresholded quantitative FFMMap: Binary representation of voxel count evoked by each random segment. Segment is white/black if voxel count was larger/smaller than threshold. D. Conventional FFMMap: Visual field chart of preferred phase-mapped stimulus locations (white circles) for all voxels exceeding threshold. Random segment outlines shown for reference.

This incompetence of quantitative FFMMaps based on voxel count is not an independent issue. It is likely caused by the high variations in the number of voxels responding to different regions of the visual field, which compress the lower end of the

color scale. In practice the delineation of scotomata will be difficult without prior knowledge of the rough location of scotomata.

In contrast, the artificial scotoma can be discerned in the conventional FFMMap shown in Figure 25D. The voxel count across the visual field also appears more uniform in areas without scotoma, due to the fact that the densities of the circular symbols in different areas are not differentiable to our eyes once an area is completely filled in. Therefore, the tradeoff for the sensitivity to scotomata of conventional FFMMap is its insensitivity to the varying voxel count across the visual field, which is a necessary component in representation of the visual function of the cortex using fMRI.

Future direction

Integration of pRF models should be the ultimate way of constructing a quantitative FFMMap. To achieve this we are facing two challenges. First, currently the amplitudes of the pRF models are normalized to the same value. Further study is needed to determine which amplitude measure (percent signal change, statistical significance and etc.) should be used to scale the amplitude of the individual pRFs. Second, the process to integrate pRF models, which best simulates the biological effect of overlapping pRFs, is not clear. A simple sum of the pRF models, the Gaussian surfaces, should be a reasonable simulation. However, more experiments or literature survey is needed to determine the limitation of this simulation.

Conclusion

The uneven representation of the visual field by voxels in visual cortex is accentuated by integrating the pRFs of voxels over each region in the visual field to

convert the conventional FMap to a quantitative form, which is required for any subsequent probability analysis. Given the large variations in the distribution of pRFs in the visual field across people, it is questionable whether any meaningful probabilistic distribution of pRFs can be generalized across people.

CHAPTER 6 SUMMARY AND FUTURE DIRECTIONS

In the four-year course of research, we completed the first two aims of this project and discovered that the third aim was not practically achievable.

For aim 1, we made detailed, quantitative comparison between conventional phase-encoded and random multifocal visual field mappings.

Randomized, multifocal mapping accurately decomposed the response of single voxels to multiple stimulus locations and made correct retinotopic assignments as noise levels increased despite decreasing sensitivity. Also, multifocal mapping became less efficient as the number of stimulus segments (locations) increased from 13 to 25 to 49 and when duty cycle was increased from 25% to 50%. Phase mapping, on the other hand, activated more extrastriate visual areas, was more time efficient in achieving statistically significant responses, and had better sensitivity as noise increased, though with an increase in systematic retinotopic mis-assignments. Overall, temporal phase mapping is likely to be a better choice for routine clinical applications though random multifocal mapping may offer some unique advantages for select applications.

For aim 2, we created a combined retinotopic mapping paradigm that takes advantage of both phase-encoded and event-related designs. The addition of the random stimuli was shown to have insignificant effect on the retinotopic mapping by the phase-encoded stimuli. Three applications were demonstrated for this combined paradigm: Simultaneous mapping the retinotopy and selected ROIs, automated calibration of the temporal phases delayed by hemodynamics, and delineation of the hemodynamic response function for each voxel responding to the random stimuli.

For aim 3, we tested the feasibility of creating a more quantitative, probability-based FMap. We derived a quantitative form of the current FMap, on

which a probability distribution could be drawn. The quantitative FFMaps from five subjects we examined showed highly variable patterns of coverage, which made it questionable whether any meaningful probabilistic distribution can be obtained. FFMaps from a large number of subjects may be needed for further study on this issue.

Based on our findings, several extensions to this study and further technical development can be executed.

Scale contrast of the combined stimuli to reflect the linearity

We designed the combined visual stimuli to achieve perceptual separation of the phase-encoded and event-related stimuli without taking into account the actual contrast values. However, theoretically the contrast level should be adjusted so that overlapped stimuli have a contrast level twice that of each of the component stimulus, to match the linear assumption the post-processing FIR model takes. This deed is expected to help with the separation of the signals evoked by phase-encoded and event-related stimuli, which is a premise for all subsequence processing.

Other possible combined stimuli

The successful separation of the phase-encoded and event-related signal evoked by the combined stimuli demonstrated in the study showed the possibility of taking advantage of different stimuli by overlapping them in the visual field. One interesting design would be to combine the phase-encoded rotating wedge and expanding ring to achieve simultaneous mapping of the two dimensions and thus reduce the mapping time by half. However, the current rotating wedge and expanding ring stimuli evoke sinusoidal waveforms with the same period and therefore their respective

signals are not differentiable. Altering the period of one of the stimuli should be sufficient to enable the combination of the two stimuli into one scan run.

Further experiments with quantitative FFMaps

Although the quantitative FFMaps of the five subjects we tested have highly variable distributions of pRFs, it is still possible that a common pattern of the distribution across people can be revealed by examination of a large number of subjects. Direct integration of neighboring pRFs of the conventional FFMap instead of plotting the voxel count to each segment from the random multifocal mapping might also show some difference in the distribution of pRFs.

Since the variations in pRF distributions likely originated from the hemodynamics underlying BOLD signals, calibrated fMRI techniques that dissociate neural signals from the hemodynamics might be able to provide more uniform FFMaps (Hoge, 2012).

REFERENCE

- Amano, K., Wandell, B.A., Dumoulin, S.O., 2009. Visual field maps, population receptive field sizes, and visual field coverage in the human MT+ complex. *J Neurophysiol* 102, 2704-2718.
- Amaro, E., Jr., Barker, G.J., 2006. Study design in fMRI: basic principles. *Brain Cogn* 60, 220-232.
- Appelbaum, L.G., Wade, A.R., Vildavski, V.Y., Pettet, M.W., Norcia, A.M., 2006. Cue-invariant networks for figure and background processing in human visual cortex. *J Neurosci* 26, 11695-11708.
- Arcaro, M.J., McMains, S.A., Singer, B.D., Kastner, S., 2009. Retinotopic organization of human ventral visual cortex. *J Neurosci* 29, 10638-10652.
- Bandettini, P.A., 2012. Twenty years of functional MRI: the science and the stories. *Neuroimage* 62, 575-588.
- Bandettini, P.A., Jesmanowicz, A., Wong, E.C., Hyde, J.S., 1993. Processing strategies for time-course data sets in functional MRI of the human brain. *Magn Reson Med* 30, 161-173.
- Baseler, H.A., Brewer, A.A., Sharpe, L.T., Morland, A.B., Jagle, H., Wandell, B.A., 2002. Reorganization of human cortical maps caused by inherited photoreceptor abnormalities. *Nat Neurosci* 5, 364-370.
- Baseler, H.A., Gouws, A., Haak, K.V., Racey, C., Crossland, M.D., Tufail, A., Rubin, G.S., Cornelissen, F.W., Morland, A.B., 2011. Large-scale remapping of visual cortex is absent in adult humans with macular degeneration. *Nat Neurosci* 14, 649-655.
- Baseler, H.A., Sutter, E.E., Klein, S.A., Carney, T., 1994. The topography of visual evoked response properties across the visual field. *Electroencephalogr Clin Neurophysiol* 90, 65-81.
- Birn, R.M., Saad, Z.S., Bandettini, P.A., 2001. Spatial heterogeneity of the nonlinear dynamics in the FMRI BOLD response. *Neuroimage* 14, 817-826.
- Boynton, G.M., Engel, S.A., Glover, G.H., Heeger, D.J., 1996. Linear systems analysis of functional magnetic resonance imaging in human V1. *J Neurosci* 16, 4207-4221.
- Boynton, G.M., Engel, S.A., Heeger, D.J., 2012. Linear systems analysis of the fMRI signal. *Neuroimage* 62, 975-984.
- Buracas, G.T., Boynton, G.M., 2002. Efficient design of event-related fMRI experiments using M-sequences. *Neuroimage* 16, 801-813.

- Buxton, R.B., Uludag, K., Dubowitz, D.J., Liu, T.T., 2004. Modeling the hemodynamic response to brain activation. *Neuroimage* 23 Suppl 1, S220-233.
- Cohen, M.S., 1997. Parametric analysis of fMRI data using linear systems methods. *Neuroimage* 6, 93-103.
- Conner, I.P., Odom, J.V., Schwartz, T.L., Mendola, J.D., 2007. Retinotopic maps and foveal suppression in the visual cortex of amblyopic adults. *J Physiol* 583, 159-173.
- Cowey, A., 1964. Projection of the retina on to striate and prestriate cortex in the squirrel monkey, *Saimiri sciureus*. *Journal of Neurophysiology* 27, 366-393.
- Cox, R.W., 1996a. AFNI: Software for analysis and visualization of functional magnetic resonance neuroimages. *Computers and Biomedical Research* 29, 162-173.
- Cox, R.W., 1996b. AFNI: software for analysis and visualization of functional magnetic resonance neuroimages. *Comput Biomed Res* 29, 162-173.
- D'Esposito, M., Zarahn, E., Aguirre, G.K., 1999. Event-related functional MRI: implications for cognitive psychology. *Psychol Bull* 125, 155-164.
- Dale, A.M., 1999. Optimal experimental design for event-related fMRI. *Hum Brain Mapp* 8, 109-114.
- Dale, A.M., Buckner, R.L., 1997. Selective averaging of rapidly presented individual trials using fMRI. *Hum Brain Mapp* 5, 329-340.
- DeYoe, E.A., Carman, G., Bandettini, P., Glickman, S., Wieser, J., Cox, R., Miller, D., Neitz, J., 1996. Mapping striate and extrastriate visual areas in human cerebral cortex. *Proceedings of the National Academy of Sciences - USA* 93, 2382-2386.
- DeYoe, E.A., Ulmer, J., Mueller, W.M., Hacein-Bey, L., Szeder, V., Maciejewski, M.J., Medler, K., Reitsma, D., Mathis, J., 2011. FMRI of Human Visual Pathways. In: Faro, S., Mohamed, F.B. (Eds.), *Functional Neuroradiology: Principles and Clinical Applications*. Springer, New York, pp. 485-511.
- DeYoe, E.A., Van Essen, D.C., 1988. Concurrent processing streams in monkey visual cortex. *Trends in Neurosciences* 11, 219-226.
- Dumoulin, S.O., Wandell, B.A., 2008. Population receptive field estimates in human visual cortex. *Neuroimage* 39, 647-660.
- Duncan, R.O., Boynton, G.M., 2003. Cortical magnification within human primary visual cortex correlates with acuity thresholds. *Neuron* 38, 659-671.
- Duncan, R.O., Sample, P.A., Weinreb, R.N., Bowd, C., Zangwill, L.M., 2007a. Retinotopic organization of primary visual cortex in glaucoma: a method for comparing cortical function with damage to the optic disk. *Invest Ophthalmol Vis Sci* 48, 733-744.

- Duncan, R.O., Sample, P.A., Weinreb, R.N., Bowd, C., Zangwill, L.M., 2007b. Retinotopic organization of primary visual cortex in glaucoma: Comparing fMRI measurements of cortical function with visual field loss. *Prog Retin Eye Res* 26, 38-56.
- Engel, S.A., 2012. The development and use of phase-encoded functional MRI designs. *Neuroimage* 62, 1195-1200.
- Engel, S.A., Glover, G.H., Wandell, B.A., 1997. Retinotopic organization in human visual cortex and the spatial precision of functional MRI. *Cerebral Cortex* 7, 181-192.
- Engel, S.A., Rumelhart, D.E., Wandell, B.A., Lee, A.T., Glover, G.H., Chichilnisky, E., Shadlen, M.N., 1994. fMRI of human visual cortex. *Nature* 369, 525.
- Felleman, D.J., Van Essen, D.C., 1991. Distributed hierarchical processing in the primate cerebral cortex. *Cerebral Cortex* 1, 1-47.
- Fishman, R.S., 1997. Gordon Holmes, the cortical retina, and the wounds of war. The seventh Charles B. Snyder Lecture. *Doc Ophthalmol* 93, 9-28.
- Fox, P.T., Miezin, F.M., Allman, J.M., Van Essen, D.C., Raichle, M.E., 1987. Retinotopic organization of human visual cortex mapped with positron-emission tomography. *Journal of Neuroscience* 7, 913-922.
- Freeman, J., Brouwer, G.J., Heeger, D.J., Merriam, E.P., 2011. Orientation decoding depends on maps, not columns. *J Neurosci* 31, 4792-4804.
- Gu, H., Stein, E.A., Yang, Y., 2005. Nonlinear responses of cerebral blood volume, blood flow and blood oxygenation signals during visual stimulation. *Magn Reson Imaging* 23, 921-928.
- Handwerker, D.A., Ollinger, J.M., D'Esposito, M., 2004. Variation of BOLD hemodynamic responses across subjects and brain regions and their effects on statistical analyses. *Neuroimage* 21, 1639-1651.
- Hansen, K.A., David, S.V., Gallant, J.L., 2004. Parametric reverse correlation reveals spatial linearity of retinotopic human V1 BOLD response. *Neuroimage* 23, 233-241.
- Hansen, K.A., Kay, K.N., Gallant, J.L., 2007. Topographic organization in and near human visual area V4. *J Neurosci* 27, 11896-11911.
- Harvey, B.M., Dumoulin, S.O., 2011. The relationship between cortical magnification factor and population receptive field size in human visual cortex: constancies in cortical architecture. *J Neurosci* 31, 13604-13612.
- Henriksson, L., Raninen, A., Nasanen, R., Hyvarinen, L., Vanni, S., 2007. Training-induced cortical representation of a hemianopic hemifield. *J Neurol Neurosurg Psychiatry* 78, 74-81.

- Hoffmann, M.B., Tolhurst, D.J., Moore, A.T., Morland, A.B., 2003. Organization of the visual cortex in human albinism. *J Neurosci* 23, 8921-8930.
- Hoge, R.D., 2012. Calibrated fMRI. *Neuroimage* 62, 930-937.
- Horton, J.C., 1992. The central visual pathways. In: Hart, W.H. (Ed.), *Adler's physiology of the eye*. Mosby Year book, St. Louis, pp. 728-772.
- Huang, R.S., Sereno, M.I., 2007. Dodecapus: An MR-compatible system for somatosensory stimulation. *Neuroimage* 34, 1060-1073.
- Hubel, D.H., Wiesel, T.N., 1965. Receptive fields and functional architecture in two nonstriate areas (18 and 19) of the cat. *Journal of Neurophysiology* 28, 229-289.
- Hubel, D.H., Wiesel, T.N., 2004. *Brain and Visual Perception: The Story of a 25-Year Collaboration*. Oxford University Press.
- Janik, J., Ropella, K.M., DeYoe, E.A., 2013. Distortions in human brain maps measured with fMRI: Visual cortex. *Human Brain Mapping*.
- Janik, J.J., Ropella, K.M., DeYoe, E.A., 2003. Distortions of human retinotopy obtained with temporal phase mapped fMRI. *Society for Neuroscience Abstracts*.
- Kandel, E.R., Schwarzh, J.H., Jessel, T.M., 1991. *Principles of Neural Science*, 4th ed. McGraw-Hill, New York.
- Kastner, S., De Weerd, P., Pinsk, M.A., Elizondo, M.I., Desimone, R., Ungerleider, L.G., 2001. Modulation of sensory suppression: implications for receptive field sizes in the human visual cortex. *J Neurophysiol* 86, 1398-1411.
- Kay, K.N., David, S.V., Prenger, R.J., Hansen, K.A., Gallant, J.L., 2008. Modeling low-frequency fluctuation and hemodynamic response timecourse in event-related fMRI. *Hum Brain Mapp* 29, 142-156.
- Krings, T., Reinges, M.H., Foltys, H., Cosgrove, G.R., Thron, A., 2001. Multimodality neuroimaging: research and clinical applications. *Neurol Clin Neurophysiol* 2001, 2-11.
- Lagarias, J.C., Reeds, J.A., Wright, M.H., Wright, P.E., 1998. Convergence Properties of the Nelder-Mead Simplex Method in Low Dimensions. *SIAM Journal of Optimization* 9, 112-147.
- Levin, N., Dumoulin, S.O., Winawer, J., Dougherty, R.F., Wandell, B.A., 2010. Cortical maps and white matter tracts following long period of visual deprivation and retinal image restoration. *Neuron* 65, 21-31.
- Levy, I., Hasson, U., Avidan, G., Hendler, T., Malach, R., 2001. Center-periphery organization of human object areas. *Nat Neurosci* 4, 533-539.

- Liu, T.T., 2012. The development of event-related fMRI designs. *Neuroimage* 62, 1157-1162.
- Liu, Z., He, B., 2008. fMRI-EEG integrated cortical source imaging by use of time-variant spatial constraints. *Neuroimage* 39, 1198-1214.
- Logothetis, N.K., 2002. The neural basis of the blood-oxygen-level-dependent functional magnetic resonance imaging signal. *Philos Trans R Soc Lond B Biol Sci* 357, 1003-1037.
- Logothetis, N.K., 2008. What we can do and what we cannot do with fMRI. *Nature* 453, 869-878.
- Logothetis, N.K., Pauls, J., Augath, M., Trinath, T., Oeltermann, A., 2001. Neurophysiological investigation of the basis of the fMRI signal. *Nature* 412, 150-157.
- Ltd, S.R., EyeLink II User Manual.
- Lund, T.E., Madsen, K.H., Sidaros, K., Luo, W.L., Nichols, T.E., 2006. Non-white noise in fMRI: does modelling have an impact? *Neuroimage* 29, 54-66.
- Ma, Y., Ward, B.D., Ropella, K.M., DeYoe, E.A., 2013. Comparison of Randomized Multifocal Mapping and Temporal Phase Mapping of Visual Cortex for Clinical Use. *Neuroimage: Clinical* (In revision).
- Marr, D., 1982. *Vision*. W.H. Freeman & Co, San Francisco.
- Martin, T., Das, A., Huxlin, K.R., 2012. Visual cortical activity reflects faster accumulation of information from cortically blind fields. *Brain* 135, 3440-3452.
- McKeefry, D.J., Gouws, A., Burton, M.P., Morland, A.B., 2009. The noninvasive dissection of the human visual cortex: using FMRI and TMS to study the organization of the visual brain. *Neuroscientist* 15, 489-506.
- Muckli, L., Naumer, M.J., Singer, W., 2009. Bilateral visual field maps in a patient with only one hemisphere. *Proc Natl Acad Sci U S A* 106, 13034-13039.
- Ogawa, S., Lee, T., Nayak, S., Glynn, P., 1990a. Oxygenation-sensitive contrast in magnetic resonance image of rodent brain in high magnetic fields. *Magnetic Resonance in Medicine* 14, 68-78.
- Ogawa, S., Lee, T.M., Kay, A.R., Tank, D.W., 1990b. Brain magnetic resonance imaging with contrast dependent on blood oxygenation. *Proceedings of the National Academy of Sciences USA* 87, 9868-9872.
- Ogawa, S., Tso-Ming, L., 1990. Magnetic resonance imaging of blood vessels at high fields: In vivo and in vitro measurements and image simulation. *Magnetic Resonance in Medicine* 16, 9-18.

- Petersen, S.E., Dubis, J.W., 2012. The mixed block/event-related design. *Neuroimage* 62, 1177-1184.
- Puckett, A.M., Mathis, J., DeYoe, E.A., 2013. An investigation of positive and inverted hemodynamic impulse response functions across multiple visual areas. *Hum Brain Mapp* In review.
- Robson, M.D., Dorosz, J.L., Gore, J.C., 1998. Measurements of the temporal fMRI response of the human auditory cortex to trains of tones. *Neuroimage* 7, 185-198.
- Saad, Z.S., DeYoe, E.A., Ropella, K.M., 2003. Estimation of FMRI response delays. *Neuroimage* 18, 494-504.
- Saad, Z.S., Ropella, K.M., Cox, R.W., DeYoe, E.A., 2001. Analysis and use of FMRI response delays. *Hum Brain Mapp* 13, 74-93.
- Sack, A.T., Linden, D.E., 2003. Combining transcranial magnetic stimulation and functional imaging in cognitive brain research: possibilities and limitations. *Brain Res Brain Res Rev* 43, 41-56.
- Sanchez-Panchuelo, R.M., Francis, S., Bowtell, R., Schluppeck, D., 2010. Mapping human somatosensory cortex in individual subjects with 7T functional MRI. *J Neurophysiol* 103, 2544-2556.
- Schira, M.M., Tyler, C.W., Spehar, B., Breakspear, M., 2010. Modeling magnification and anisotropy in the primate foveal confluence. *PLoS Comput Biol* 6, e1000651.
- Schira, M.M., Wade, A.R., Tyler, C.W., 2007. Two-dimensional mapping of the central and parafoveal visual field to human visual cortex. *J Neurophysiol* 97, 4284-4295.
- Sereno, M.I., Dale, A.M., Reppas, J.B., Kwong, K.K., Belliveau, J.W., Brady, T.J., Rosen, B.R., Tootell, R.B.H., 1995. Borders of multiple visual areas in humans revealed by functional MRI. *Science* 268, 889-893.
- Singh, K.D., 2012. Which "neural activity" do you mean? fMRI, MEG, oscillations and neurotransmitters. *Neuroimage* 62, 1121-1130.
- Sinha, P., Meng, M., 2012. Superimposed hemifields in primary visual cortex of achiasmic individuals. *Neuron* 75, 353-355.
- Slotnick, S.D., Klein, S.A., Carney, T., Sutter, E., Dastmalchi, S., 1999. Using multi-stimulus VEP source localization to obtain a retinotopic map of human primary visual cortex. *Clin Neurophysiol* 110, 1793-1800.
- Smith, A.T., Singh, K.D., Williams, A.L., Greenlee, M.W., 2001. Estimating receptive field size from fMRI data in human striate and extrastriate visual cortex. *Cereb Cortex* 11, 1182-1190.
- Smith, M.M., Strottmann, J.M., 2001. Imaging of the optic nerve and visual pathways. *Semin Ultrasound CT MR* 22, 473-487.

- Striem-Amit, E., Hertz, U., Amedi, A., 2011. Extensive cochleotopic mapping of human auditory cortical fields obtained with phase-encoding fMRI. *PLoS ONE* 6, e17832.
- Sunness, J.S., Liu, T., Yantis, S., 2004. Retinotopic mapping of the visual cortex using functional magnetic resonance imaging in a patient with central scotomas from atrophic macular degeneration. *Ophthalmology* 111, 1595-1598.
- Sutter, E.E., 2001. Imaging visual function with the multifocal m-sequence technique. *Vision Res* 41, 1241-1255.
- Swisher, J.D., Gatenby, J.C., Gore, J.C., Wolfe, B.A., Moon, C.H., Kim, S.G., Tong, F., 2010. Multiscale pattern analysis of orientation-selective activity in the primary visual cortex. *J Neurosci* 30, 325-330.
- Swisher, J.D., Halko, M.A., Merabet, L.B., McMains, S.A., Somers, D.C., 2007. Visual topography of human intraparietal sulcus. *J Neurosci* 27, 5326-5337.
- Tabuchi, H., Yokoyama, T., Shimogawara, M., Shiraki, K., Nagasaka, E., Miki, T., 2002. Study of the visual evoked magnetic field with the m-sequence technique. *Invest Ophthalmol Vis Sci* 43, 2045-2054.
- Talbot, S.A., Marshall, W.H., 1941. Physiological studies on neural mechanisms of visual localization and discrimination. *American Journal of Ophthalmology* 24, 1255-1264.
- Taylor, M.J., Donner, E.J., Pang, E.W., 2012. fMRI and MEG in the study of typical and atypical cognitive development. *Neurophysiol Clin* 42, 19-25.
- Tootell, R.B., Silverman, M.S., Switkes, E., De Valois, R.L., 1982. Deoxyglucose analysis of retinotopic organization in primate striate cortex. *Science* 218, 902-904.
- Tootell, R.B.H., Mendola, J.D., Hadjikhani, N.K., Ledden, P.J., Liu, A.K., Reppas, J.B., Sereno, M.I., Dale, A.M., 1997. Functional analysis of V3A and related areas in human visual cortex. *Journal of Neuroscience* 17, 7060-7078.
- Tusa, R.J., Palmer, L.A., Rosenquist, A.C., 1978. The retinotopic organization of area 17 (striate cortex) in the cat. *Journal of Comparative Neurology* 177, 213-236.
- Ungerleider, L.G., Mishkin, M., Goodale, M.A., Mansfield, R.J.W., 1982. Two cortical visual systems. In: Ingle, D.J. (Ed.), *Analysis of Visual Behavior*. MIT Press, Cambridge, MA, pp. 549-586.
- Van Essen, D.C., 2003. Organization of Visual Areas in Macaque and Human Cerebral Cortex. In: Chalupa, L.M., Werner, J.S. (Eds.), *The visual neuroscience*. A Bradford Book.
- Van Essen, D.C., Drury, H.A., Dickson, J., Harwell, J., Hanlon, D., Anderson, C.H., 2001. An integrated software suite for surface-based analyses of cerebral cortex. *J Am Med Inform Assoc* 8, 443-459.

- Van Essen, D.C., Zeki, S.M., 1978. The topographic organization of rhesus monkey prestriate cortex. *Journal of Physiology* 277, 193-226.
- Vanni, S., Henriksson, L., James, A.C., 2005. Multifocal fMRI mapping of visual cortical areas. *Neuroimage* 27, 95-105.
- Vuori, E., Vanni, S., Henriksson, L., Tervo, T.M., Holopainen, J.M., 2012. Refractive surgery in anisometropic adult patients induce plastic changes in primary visual cortex. *Acta Ophthalmol* 90, 669-676.
- Wandell, B.A., Brewer, A.A., Dougherty, R.F., 2005. Visual field map clusters in human cortex. *Philos Trans R Soc Lond B Biol Sci* 360, 693-707.
- Wandell, B.A., Dumoulin, S.O., Brewer, A.A., 2007. Visual field maps in human cortex. *Neuron* 56, 366-383.
- Wandell, B.A., Winawer, J., 2011. Imaging retinotopic maps in the human brain. *Vision Res* 51, 718-737.
- Ward, B.D., 2006. Deconvolution Analysis of FMRI Time Series Data. AFNI Documentation.
- Ward, B.D., Janik, J., Mazaheri, Y., Ma, Y., Deyoe, E.A., 2012. Adaptive Kalman filtering for real-time mapping of the visual field. *Neuroimage* 59, 3533-3547.
- Winawer, J., Horiguchi, H., Sayres, R.A., Amano, K., Wandell, B.A., 2010. Mapping hV4 and ventral occipital cortex: the venous eclipse. *J Vis* 10, 1.
- Zeki, S.M., 1971. Cortical projections from two prestriate areas in the monkey. *Brain Research* 34, 19-35.